Journal of South American Earth Sciences 94 (2019) 102238

Contents lists available at ScienceDirect

Journal of South American Earth Sciences

journal homepage: www.elsevier.com/locate/jsames

Miocene fragmentation of the Central Andean foreland basins between 26 and 28°S

S. Zapata[a,*], E.R. Sobel[a], C. del Papa[b], C. Muruaga[c], R. Zhou[d]

[a] University of Potsdam, Potsdam, Brandenburg, Germany
[b] Cicterra, CONICET-University of Cordoba, Cordoba, Argentina
[c] Instituto de Sedimentología, Fundación Miguel Lillo, Tucumán, Argentina
[d] School of Earth and Environmental Sciences, The University of Queensland, St Lucia, QLD 4072, Australia

ARTICLE INFO

Keywords:
Foreland basin fragmentation
Andean retroarc
Mountain building

ABSTRACT

We present new U-Pb LA-ICP-MS data from the Central Andean foreland basins combined with new and published stratigraphic information in order to reconstruct the Miocene fragmentation of the Andean foreland between 26 and 28°S. The disruption of this foreland basin and the subsequent development of elevated intermountain basins have been the focus of several studies. However, the absence of temporal constraints in the Miocene to Pliocene sedimentary record of the low elevation Choromoro and Tucuman foreland basins has presented an obstacle for precise paleogeographic reconstructions. We describe 11 discontinuous stratigraphic sections and use the U-Pb LA-ICP-MS method to date 10 pyroclastic-bearing sediments in order to reconstruct the stratigraphic evolution of the Choromoro and Tucuman basins. We combine our results with published stratigraphic and thermochronologic data from adjacent basins to present a refined Miocene paleogeographic model. In a first stage, a continuous Early Miocene foreland lacustrine basin developed, filling up the preexisting Paleogene topography. The second stage is characterized by basin unroofing around ~12 Ma; the easily eroded sedimentary cover was removed, leading to the uplift of the underlying basement rocks and the segmentation of the lacustrine system. In the third stage, relief increase took place after ~6 Ma due to the low erodibility of the basement blocks; as a result, stable fluvial systems developed. Progressive relief development caused pronounced unconformities in the basins and the development of proximal fluvial-gravitational depositional systems after 3 Ma. This model emphasizes on the relations between tectonics, climate, and erodibility, and their control on the evolution of the depositional systems and relief.

1. Introduction

Complex interactions between tectonics, climate, and rock erodibility control the development of topographic relief (e.g. Allen, 2008; Roe et al., 2008; Sobel et al., 2003). Mountain building occurs when erosion is overcome by tectonically-driven rock uplift. Erosional efficiency is controlled by climate, rock erodability, and relief, while rock uplift is primarily related to tectonics (e.g. England and Molnar, 1990; Pingel et al., 2014; Roe et al., 2006; Sobel and Strecker, 2003; Whipple, 2009; Willett, 1999). In foreland basins, mountain building phases are often associated with a forelandward progression of deformation, which leads to the fragmentation of these foreland basins (DeCelles and Giles, 1996; e.g. Hain et al., 2011; Mortimer et al., 2007). The response of the depositional systems to basin fragmentation includes regressive sedimentary cycles, changes in sources areas and sediment supply, variation in the local climates, and the formation of stratigraphic unconformities (e.g. Fosdick et al., 2017; Horton and DeCelles, 1997; del Papa et al., 2013; Pingel et al., 2014). Contractional foreland basins in the Central Andes formed during the Cenozoic and were subsequently deformed and fragmented (Horton, 2018; Löbens et al., 2013; Mortimer et al., 2007; Sobel et al., 2003).

Between 26 and 28°S, the basement-cored ranges now constitute an effective orographic barrier responsible for an east-west precipitation gradient (Fig. 1c). This orographic barrier separates the elevated intermountain basins on the arid western side from the low-elevation foreland basins on the humid side. At these latitudes, many studies have focused on the tectonic evolution and the Miocene fragmentation of the Andean retroarc (e.g. Bonini et al., 2017; Bossi and Muruaga, 2009; Coutand et al., 2006; Iaffa et al., 2011a,b; Kleinert and Strecker, 2001; Löbens et al., 2013; Mortimer et al., 2007; Muruaga, 2001; Pratt et al., 2008; Sobel and Strecker, 2003). On the arid side, more continuous exposures have facilitated numerous stratigraphic and

* Corresponding author.
E-mail addresses: szapatah@gmail.com, ZapataS@si.edu (S. Zapata).

https://doi.org/10.1016/j.jsames.2019.102238
Received 21 April 2019; Received in revised form 18 June 2019; Accepted 18 June 2019
Available online 21 June 2019
0895-9811/

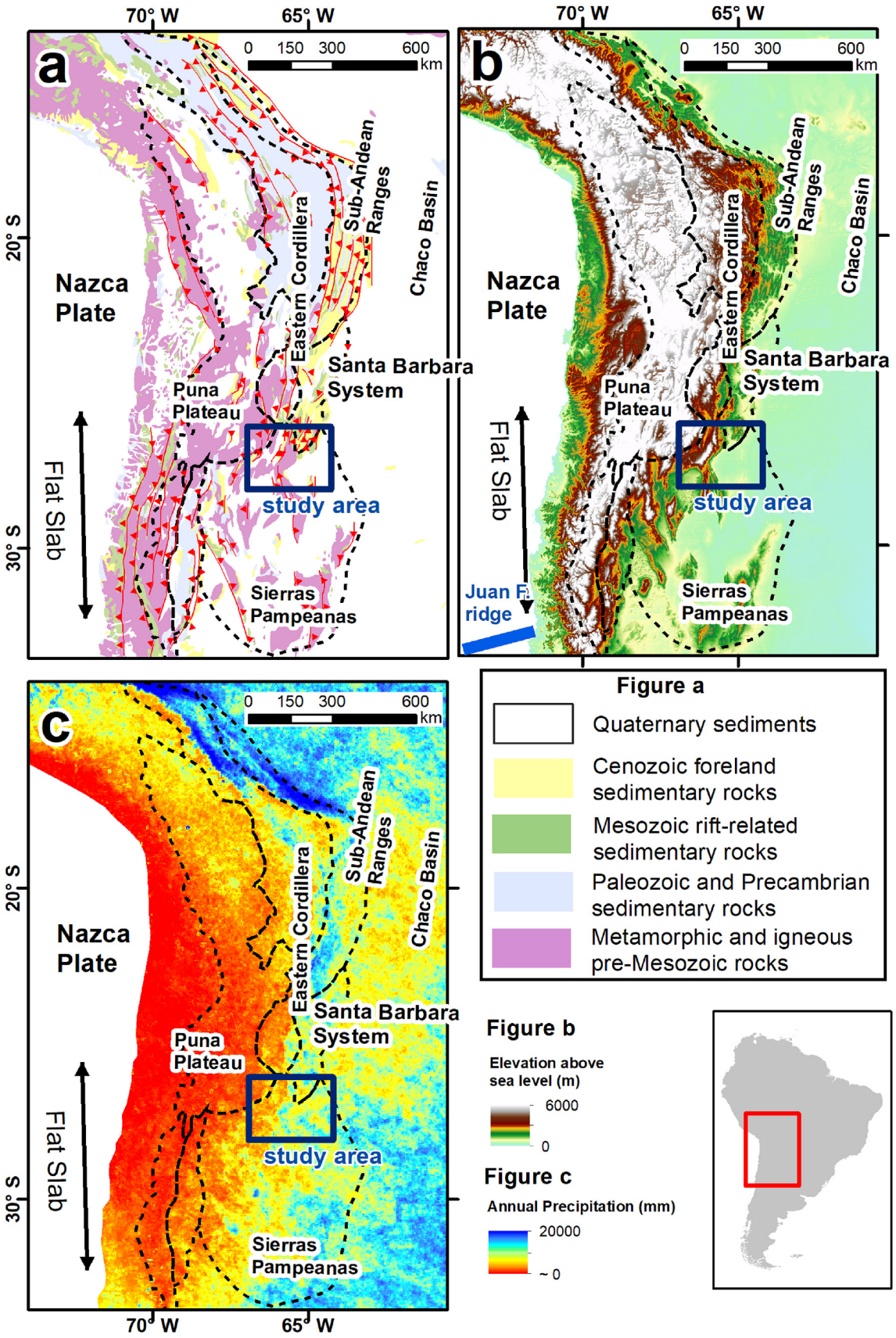

Fig. 1. (a) Central Andean sedimentary cover and geological provinces modified from Kley et al. (1999). (b) Digital elevation model from GTOPO30 data. (c) Mean annual precipitation from satellite tropical rainfall mission (TRMM) (NASA, 1997).

geochronological studies (e.g. Bonini et al., 2017; Bossi et al., 2001; Kleinert and Strecker, 2001; Mortimer et al., 2007; Spagnuolo et al., 2015). In contrast, on the humid side, the discontinuous Miocene outcrops and the lack of temporal and stratigraphic constraints have limited precise stratigraphic correlations and refined source to sink analyses (Iaffa et al., 2011a,b; Löbens et al., 2013; Sobel et al., 2003). Nevertheless, several studies have documented coarsening-up successions correlatable with the units on the dry side (e.g. Bossi et al., 1998; Gavriloff and Bossi, 1992; Georgieff et al., 2014).

In this contribution, we present logs from 11 partial stratigraphic sections, 10 new detrital zircon U-Pb ages from volcaniclastic-bearing sandstones, and sedimentary provenance data to reconstruct the Miocene-Pliocene evolution of the basins in the humid foreland between 26 and 28°S. We combine our results with published low-temperature thermochronologic data sets, and detailed basin reconstructions from the western arid side to produce a refined paleogeographic model, subdivided into three main stages. This model highlights the response of relief and depositional systems to interactions between tectonics, climate, and rock erodibility during contractional phases.

2. Geological background

The Cenozoic compressional setting of the Central Andes varied over time and along-strike. Reasons proposed for this variability include changes in the convergence rate between the South American and the Nazca plates, changes in the coupling between the plates, and penetration of the subducting slab into the mantle (Chen et al., 2019; Horton, 2018; Oncken et al., 2006; Ramos, 1999). During the Cenozoic compressional phases, several flexural foreland basins were developed along the Andean retroarc due to the growth of topographic loads farther west. During the subsequent deformational phases, previously-formed foreland basins were fragmented and deformed, leading to basin compartmentalization and the formation of elevated intermountain basins (e.g. Coutand et al., 2006; Pingel et al., 2014; Zhou et al., 2017).

Between 26 and 28°S, the high elevation Puna Plateau, and the Santa Bárbara system transition into the Sierras Pampeanas tectonomorphic province (Fig. 1a). The Santa Barbara system comprises a broken foreland basin characterized by the inversion of inherited normal faults. The Sierras Pampeanas broken foreland is characterized by discontinuous basement ranges bounded by high angle basement faults (Fig. 1a). In this region, the Andean retroarc includes the Aconquija and the Cumbres Calchaquies ranges, which are ~5000 masl basement highs. These ranges are also responsible for a pronounced rainfall gradient, which produces a humid climate to the east and a dry climate to the west. These orographic barriers also separate the elevated (~2200 masl) intermountain basins in the west from the low elevation (~1000 masl) foreland basins (Figs. 1b and 2).

The stratigraphic record of the arid western side is preserved in the Campo Arenal, Villavil, El Cajon, and the Santa Maria basins (Figs. 2 and 3) (Bonini et al., 2017; Bossi and Muruaga, 2009; Bossi and Palma, 1982; Kleinert and Strecker, 2001; Mortimer et al., 2007). These basins are characterized by 1.5–3.0 km of Miocene to Pliocene strata unconformable deposited on top of the crystalline basement or on top of a relatively thin (< 200 m) layer of Paleogene sedimentary rocks (Fig. 3) (Bossi and Muruaga, 2009; Muruaga, 2001). The Miocene sedimentary successions are characterized by coarsening-up lacustrine and fluvial systems. The Pliocene sediments were deposited in proximal fluvial depositional systems on top of a pronounced erosive unconformity with the Miocene sedimentary successions (Bonini et al., 2017; Bossi and Muruaga, 2009; Kleinert and Strecker, 2001; Pratt et al., 2008; Spagnuolo et al., 2015). The Campo-Arenal basin is also characterized by Miocene (12–7 Ma) extrusive and subvolcanic rocks and their plutonic equivalents, grouped into the Farallón Negro volcanic complex (Halter et al., 2004; Harris et al., 2004). The slightly younger (~10–5 Ma) Agua Rica plutonic complex has been described at the southern end of the Aconquija range (Fig. 2) (Landtwing et al., 2002).

On the humid foreland side, a similar Miocene-Pliocene stratigraphic record has been described in the Choromoro and the Tucuman basins (Fig. 3). In the Choromoro basin, the Miocene units unconformably overlay Cretaceous and Paleogene sedimentary rocks. The lowermost Miocene unit is the Río Salí Fm., which is composed of fine-grained sedimentary rocks deposited in a lacustrine depositional system (Gavriloff and Bossi, 1992; Georgieff et al., 2014). This is overlain by the India Muerta Fm., which is composed of fine to medium-grained sandstones deposited in a fluvial system (Bossi, 1969; Georgieff et al., 2014). Finally, conglomeratic beds of the Ticucho Fm. are unconformably deposited on top of the India Muerta Fm. (Bossi, 1969; Georgieff et al., 2014; González, 2000).

In the Tucuman basin, stratigraphic exposures are scarce. However, the available outcrops and the subsurface seismic data suggest a stratigraphic record similar to the Choromoro basin (Fig. 3) (Georgieff et al., 2014; Iaffa et al., 2011a,b). The Miocene record in the Tucuman basin is compose of the Guasayan and Aconquija formations (Bossi et al., 1998; Mon and Urdaneta, 1972). Authors have assigned an Eocene age for the Aconquija Fm. based on two K-Ar radiometric ages of ashes (Dal Molin et al., 2003).

An extensive low-temperature thermochronologic database has been obtained and modeled in the humid part of the study area (Coutand et al., 2006; Löbens et al., 2013; Mortimer et al., 2007; Sobel et al., 2003; Zapata et al., 2018). The Aconquija range is characterized by Miocene and Pliocene (15-3 Ma) apatite (U-Th-Sm)/He (AHe) and apatite fission track (AFT) ages. To the north of the Tucuman massif, Miocene AHe ages have also been reported (Fig. 2) (Löbens et al., 2013; Sobel and Strecker, 2003; Zapata et al., 2018). The remaining basement blocks in the study area are characterized by Mesozoic AFT ages and Cretaceous to Paleogene AHe ages (Coutand et al., 2006; Löbens et al., 2013; Mortimer et al., 2007; Sobel et al., 2003; Zapata et al., 2018). Thermal modeling of the ranges reveals the timing of cooling episodes. Jurassic to Cretaceous cooling above 120 °C is related to extensional rifting events. Paleogene exhumation occurred in the San Javier range, Altos del Totora, and Eastern ranges (Zapata et al., 2018). The other ranges experienced Miocene reheating and exhumation.

3. Methods

3.1. Sampling and field methods

Lack of structural relief and dense vegetation related to the humid climate in the Choromoro and the Tucuman basins present challenges for measuring and describing the stratigraphy. In the absence of continuous exposures of the studied units, eleven partial stratigraphic segments were independently described. These segments were interpreted and correlated using the described sedimentary facies, the relative structural positions, and U-Pb LA-ICP-MS zircon ages from interbedded pyroclastic materials.

3.2. Sandstone petrography and conglomerate clast counting

Conglomerate clast counting was performed following the ribbon counting method (Howard, 1993). Clasts < 2 cm in size were excluded from the analysis. At least 300 points were counted in the sandstone samples following the Gazzi-Dickinson method presented in Dickinson (1985).

3.3. U-Pb LA-ICP-MS procedures

We collected pyroclastic material and separated zircons using standard density and magnetic methods. The zircon 91500, which has a $^{206}Pb/^{238}U$ age of 1062.4 ± 0.4 Ma and $^{206}Pb/^{207}Pb$ age of 1065.4 ± 0.3 Ma was used as the primary reference material (Wiedenbeck et al., 1995). TEMORA2 and Fish Canyon Tuff zircons

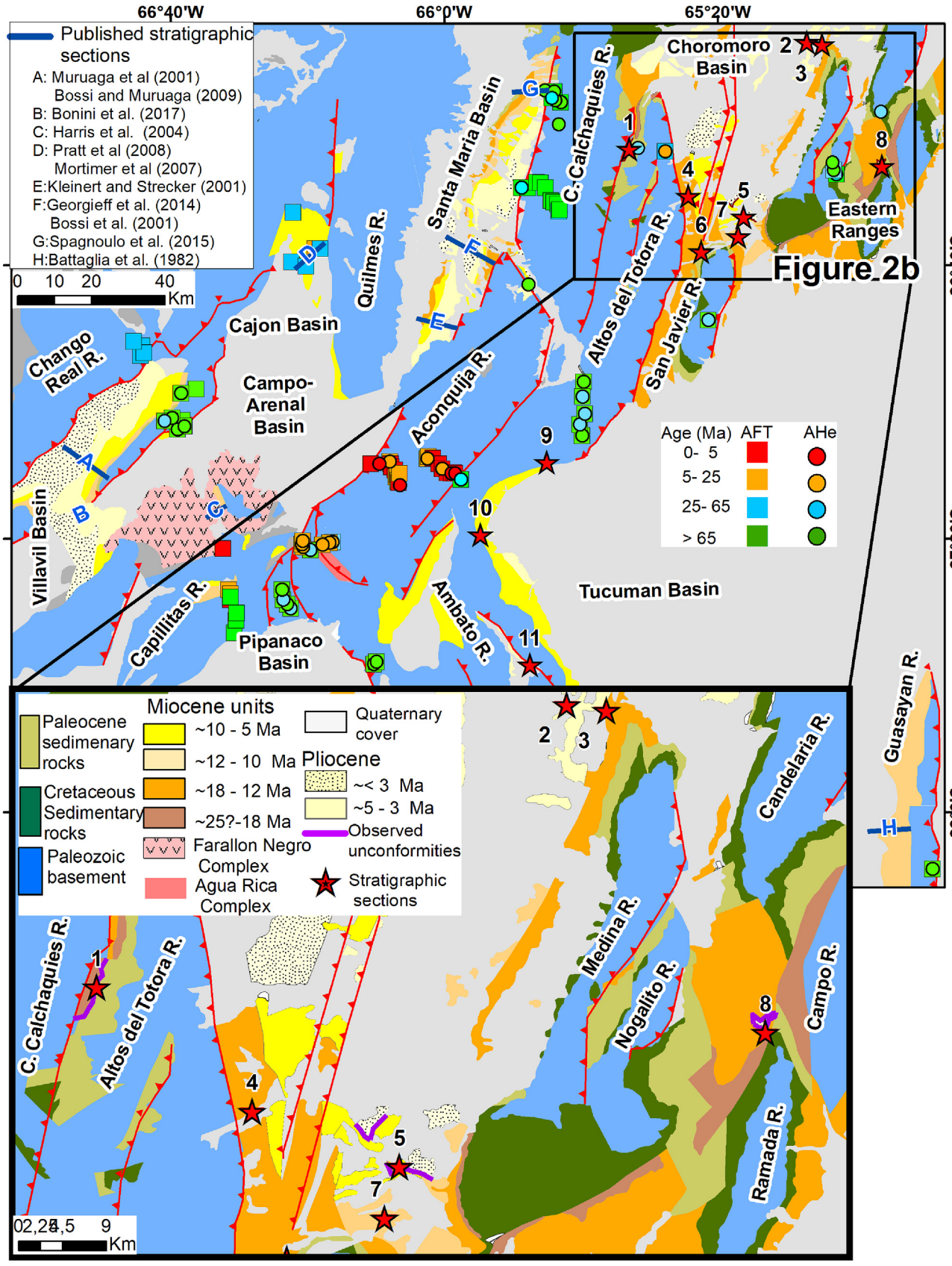

(caption on next page)

Fig. 2. Geological map of the study area modified from González et al. (2000) and available thermochronology ages (Coughlin et al., 1999; Coutand et al., 2006; Dal Molin et al., 2003; Georgieff et al., 2014; Iban et al., 2001; Löbens et al., 2013; Mortimer et al., 2007; Sobel and Strecker, 2003). Color code denotes ages; squares represent AFT, circles are AHe. Blue lines and blue labels denote previously published stratigraphic sections (Bonini et al., 2017; Bossi and Muruaga, 2009, Dal Molin et al., 2003; Harris et al., 2004; Kleinert and Strecker, 2001; Mortimer et al., 2007; Spagnuolo et al., 2015). Red stars represent the eleven stratigraphic sections presented in this contribution. 1: Rearte River, 2 and 3: Ruta 9 – Candelaria road, 4: Vipos River, 5: India Muerta River, 6: San Javier - Tapia road, 7: Tapia River, 8: Nio River, 9: Monteros - Pueblo Viejo road, 10: Cochuna River, and 11: La Escaba Dam. (For interpretation of the references to color in this figure legend, the reader is referred to the Web version of this article.)

were used as secondary reference materials.

Laser ablation was achieved using an ASI RESOlution 193 ArF nm excimer laser system. Following the evacuation of air, He carrier gas was introduced into the laser cell at a flow rate of 0.35 l/min. 0.005 l/min of N^2 gas was also introduced to the laser cell to enhance the measurement sensitivity. The gas mixture was then introduced into the plasma torch of a Thermo iCAP RQ quadruple ICPMS with 0.85 l/min Ar nebulizer gas. No reaction gas was employed. The laser was run with a 30-μm diameter round spot at 10 Hz, with a measuring instrument laser-fluence (laser pulse energy per unit area) of 2.9 J/cm^2. For each spot, 3 s of blank was collected, followed by 20 s of ablation and 5 s of wash out. Prior to data acquisition, ICP MS signals were optimized during tuning. For our session, ~550 K cps of ^{238}U counts, ~1 of ^{238}U/^{232}Th, and ~0.22 of ^{206}Pb/^{238}U were achieved for measuring NIST612 glass using line scans of 3 μm/s, 10 Hz, 50 μm round laser pit, and 3 J/cm^2. We collected the following isotopes using a single collector: 88Sr (dwell time = 0.005 s), 91Zr (dwell time = 0.001 s), 200Hg (dwell time = 0.01 s), ^{204}Pb (dwell time = 0.01 s), 206 Pb (dwell time = 0.045 s), ^{207}Pb (dwell time = 0.055 s), ^{208}Pb (dwell time = 0.01 s), 232Th (dwell time = 0.01 s), 238U (dwell time = 0.01 s). A single cycle took ~0.155 s. Therefore, during a 20-s ablation, approximately 120 measurements were made on each mass. Reduction of raw data was accomplished using the program "IOLITE" (Paton et al., 2011). No common Pb correction on 91500 zircon was undertaken.

From our measuring session, we obtained a ^{206}Pb/^{238}U age of 28.86 ± 0.16 Ma (n = 23, MSWD = 1.53) for the Fish Canyon Tuff zircon, which has a TIMS ^{206}Pb/^{238}U age of 28.40 ± 0.02 Ma (Schmitz and Bowring, 2001). We also obtained a ^{206}Pb/238U age of 420.54 ± 1.48 Ma (n = 70, MSWD = 10.6) for the TEMORA2 zircon, which has a TIMS ^{206}Pb/^{238}U age of 416.78 ± 0.33 Ma (Black et al., 2004).

Our samples present complex U-Pb zircon age distributions due to the presence of older age populations. These older ages may be related

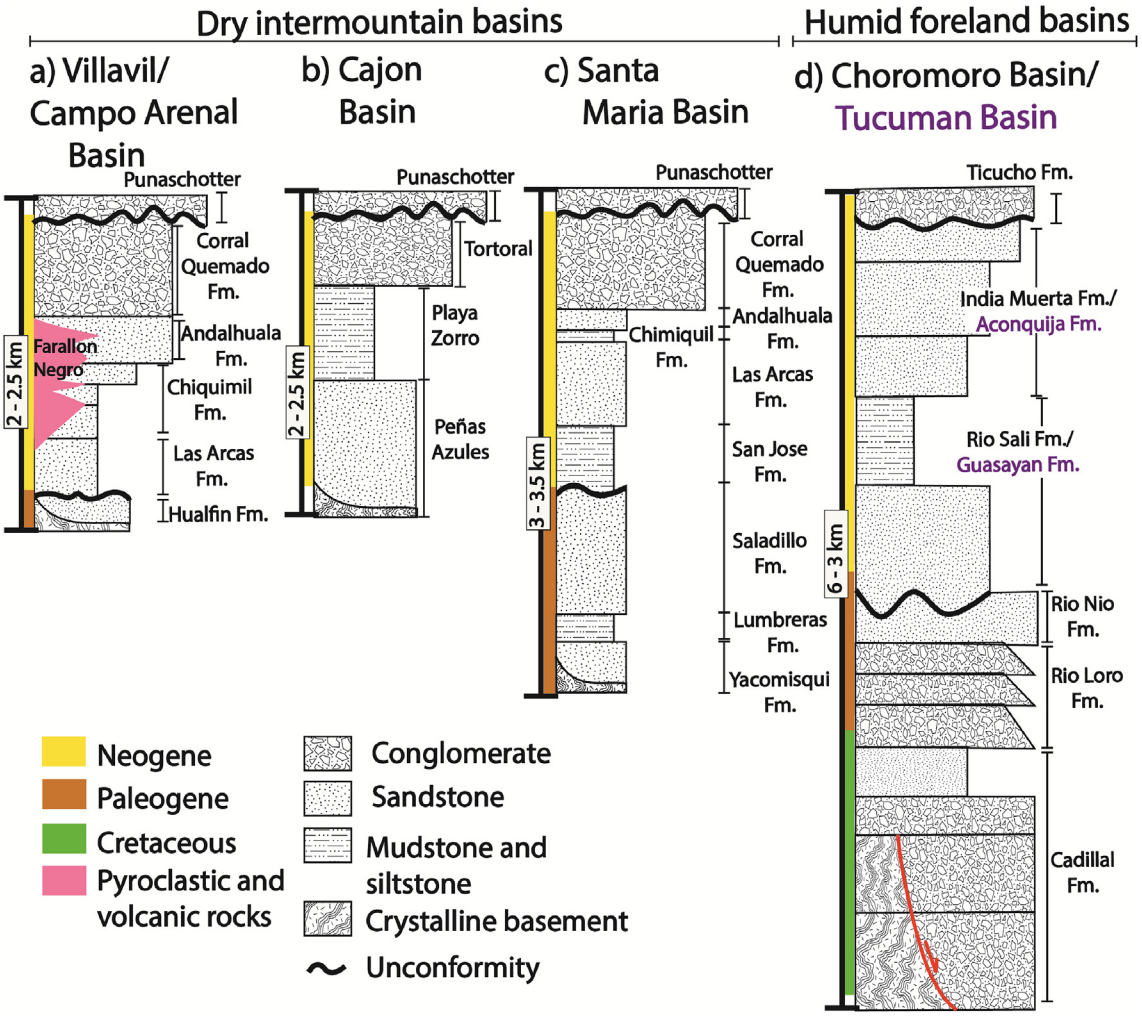

Fig. 3. Schematic stratigraphic sections in the study area. (a) Campo Arenal and Villavil basins modified from Bossi and Muruaga (2009). (b) Cajon Basin modified from Mortimer et al. (2007). (c) Santa Maria basin modified from Georgieff et al. (2014), Kleinert and Strecker (2001), and Spagnuolo et al. (2015). (d) Choromoro and Tucuman basins modified from Georgieff et al. (2014).

Table 1
Description and interpretation of sedimentary facies after Miall (2013).

Code	Description	Interpreted depositional process
Fy	Grey and red mudstones and siltstones with abundant nodules and gypsum crystals	Suspension deposition and evaporite intrasediment mineral deposition
Frh	Reddish to brownish mudstones and siltstones with horizontal lamination	Settling from suspension under oxic conditions
Fgh	Green mudstones with horizontal lamination	Suspension deposition reducing conditions
Sm	Grey and reddish massive, matrix rich, fine to coarse-grained sandstones	Hyper-concentrated flow, rapid deposition
Sw	Grey and brownish fine-grained sandstones with wavy lamination	Wave action – lower flow regimen
Sh	Yellowish fine-medium grained sandstones with horizontal lamination, fluid escape structures (dish–convolute lamination)	Unconfined plane-bed, upper flow regimen
St	Grey coarse pebbly sandstones with trough lamination	3D dune migration
Sc	Grey fine-grained to pebbly sandstones with planar-cross stratification	2D bedform migration under unidirectional flow
Sce	Medium to coarse sandstones with large-scale (> 1 m) planar cross bedding. good selection	Dune migration associated with unidirectional airflow currents
Gms	Clast-supported granule conglomerate with floating pebbles, structureless.	Sheet flow, rapid deposition
Gmm	Cobbles to boulders conglomerates, angular, poorly sorted, massive matrix supported	Gravitational debris flows
Gmv	Conglomerates, poorly sorted, massive, matrix supported, with abundant volcanic material	Gravitational pyroclastic debris flows
Gt	Clast-supported pebbly to cobbly conglomerates with trough cross-bedding	Migration of gravel bars and channel fills
Gi	Clast-supported imbricated gravels	Bed load migration, longitudinal deforms
T	Fine-grained crystal tuffs	Ash fall
Y	Coalescent crystals and nodules gypsum beds within reddish clay matrix	Evaporite mineral precipitation
Ig	Ignimbrites and volcanic breccias	High-density pyroclastic flows
P	Root traces, iron-rich layers and, carbonate nodules	Paleosols

to the interaction between the magmas and the host rocks, long pre-eruptive magmatic residence, and post-eruptive sedimentary re-working. Therefore, to obtain the age closest to sediment deposition, older grains were systematically excluded from the age calculation until we obtained mean square weighted deviated values (MSWD) lower than two. For the 3 samples without a young reproducible population, the zircon grain with the youngest age is presented as the maximum depositional age (MD).

4. Stratigraphic field relations, petrography, and paleoenvironments

We divided the Miocene-Pliocene record of the Choromoro and the Tucuman basins into six different stratigraphic sections, based on distinctive stratigraphic contacts and sedimentary facies assemblages (Tables 1 and 2). The Río Salí Fm. was divided into the lower, middle, and upper sections. The units described as the India Muerta Fm. in the Choromoro basin and the Aconquija Fm. in the Tucuman basin were divided into the lower and the upper India Muerta sections. Finally, the Pliocene Ticucho Fm. was described.

4.1. Lower Río Salí Fm

This unit unconformably overlies Paleogene rocks of the Rio Loro Fm. in the northwestern part of the Choromoro basin (Section 1, Fig. 2). This unit is constituted by the facies assemblage (I), which is dominantly composed of clast-supported, matrix-rich, massive pebbly conglomerate beds (Gms), imbricated clast-supported conglomerates (Gi), and massive coarse-grained sandstone beds (Sm); both facies exhibit granule to pebble floating clasts (Fig. 4b) (Tables 1 and 2). This facies association is characterized by 1–5 m-thick tabular and laterally continuous beds with crude stratification, organized in 10–15 m stacking packages. The facies Gms and Sm are interbedded with lenticular, scoured basal beds of imbricated conglomerate (Gi). Some layers of Gms and Sm facies present root-trace bioturbation, iron-rich layers and carbonate nodules (P).

Two samples collected in the Sm facies are characterized by 29–36% of spary carbonate cement, containing poorly sorted sub-rounded grains of monocrystalline quartz and feldspars (Table 3). Quartz and feldspar crystals are often observed within coarser grained plutonic lithics (Fig. 5b). The samples plot in the transitional continental field in the tectonic discrimination diagram of Dickinson (1985) (Fig. 5a).

The facies assemblage (I) results from a combination of different depositional processes within an ephemeral fluvial depositional system. Based on the sheet-like geometry and the absence of gradational and tractive sedimentary structures, the Gms and Sm facies are interpreted as the result of rapidly, unconfined, hyper-concentrated floods. The facies Gi represents in-channel fills associated with an ephemeral fluvial setting (Blair and McPherson, 2009; Miall, 2013). The paleosols (P) represent soil formation and biotic colonization after the abandonment of ephemeral channels.

4.2. Middle Río Salí Fm

This unit is very continuous in the Choromoro and the Tucuman basins. It conformably overlies the lower Río Salí Fm. in the NW part of the Choromoro basin (section 1, in Fig. 2). Between the Nogalito and the Campo ranges, this unit unconformably overlies rocks of the Paleogene Rio Nio Fm. (Fig. 2). The middle Río Salí Fm. is composed of three facies assemblages. The lower section is dominated by the facies assemblages (II) and (III); towards the top, these facies associations progressively transition to the facies association (IV) (Fig. 6).

The facies assemblage (II) is composed of white very well sorted medium to coarse-grained sandstones (Sce) interbedded with green mudstones (Fgh). The facies Sce is composed of 2–5 m thick, tabular well-sorted quartz-rich sandstones, with irregular to wavy lower and upper contacts (Tables 1 and 2). This facies exhibits 1–3 m thick tabular cross-bedding sets which are characterized by normal grain-sized grading laminae and by lenticular coarse-grained sandstones laminae. The facies Fgh corresponds to 0.1–0.3 m continuous and tabular beds of organic-rich laminated green mudstones (Fig. 4c).

The well-sorted quartz-rich sandstones with large-scale planar cross-bedding observed in the facies Sce are characteristic of eolian dunes (Pye and Tsoar, 2008). Fine-grained, draping sediments (Fgh) are interpreted as deposits of decantation from standing water bodies. Facies association (II) is interpreted as eolian dunes and associated wet inter-dune that forms ephemeral ponds.

Facies assemblage (III) is mainly composed of fine to coarse-grained sandstones (Sce, Sc, Sw, Sm) (Table 2). These sandstones are characterized by structureless (Sm), wavy laminated (Sw), cross laminated (Sc), and quartz-rich eolian sandstone beds (Sce). This facies association has ~0.1 m thick beds stacked in packages up to 2 m thick. Facies Sm and Sc are often characterized by scoured bases, with massive or slightly normal grading. Eolian facies (Sce) in this association have thinner beds (< 1 m) with respect to the facies assemblage II and are interbedded with facies Sm, Sc, and Sw. Sandstones facies are also

Table 2
Facies assemblage descriptions and interpretations of the depositional system.

Facies Assemblages	Lithofacies	Bed thickness (m)	Bed geometry	Interpreted depositional environment
I	P, Gms, Gi, nd Sm	1–5	Tabular and continuous in outcrop extent with some lenticular geometries	Ephemeral fluvial system
II	Sce and Fgh	2–6	Tabular and continuous in outcrop extent	Eolian dunes and interdune shallow ephemeral lakes
III	Sc, Sce, Sw, Sm, Fgh, and Frh	0.1–1	Tabular and continuous in outcrop extent, with lenticular geometries	Marginal lake deposits influenced by subaerial to subaqueous processes
IV	Sm, Fgh, and Frh	0.1–1	Tabular and continuous in outcrop extent	Fresh-water lake
V	Y, Sm, Fgh, and Frh	0.1–0.5	Tabular and continuous in outcrop extent	Ephemeral underfilled saline lacustrine mudflats and saline lake pans
VI	Sm, T, Sh, and Frh	1–5	Tabular and continuous in outcrop extent	Terminal alluvial fan or ephemeral fluvial
VII	Gt, Gc, Sm, St, and Sc	1–5	Coarse-grained, discontinuous lenticular beds	Gravelly to sandy braided fluvial
VIII	T, Ig, Gmv	0.5–3	Tabular beds and coarse-grained, discontinuous lenticular beds	Proximal to medial explosive volcanism
IX	P, Gi, Gmm	1–5	Tabular and continuous in outcrop extend with some lenticular geometries	Proximal to a medial position in fluvial dominated alluvial fan

interbedded with subordinated layers of brown to green mudstones (Fgh and Frh).

The facies assemblage (III) is interpreted to reflect different depositional processes in a transitional to marginal lake characterized by intermittent subaqueous to subaerial conditions. Facies Sc and Sm are interpreted as the result of bedload deposition from tractive unidirectional subaqueous underflows in medium to low energy settings (Marshall et al., 1979). The presence of eolian (Sce) and wavy sandstones (Sw) facies are distinctive of coastal systems influenced by the interactions of subaerial wind and subaqueous waves (Anadon et al., 1991; Bridge and Demicco, 2008).

The facies assemblage (IV) is mainly composed of 0.1–1.0 m-thick beds of interbedded green (Fgh), red to brown siltstones (Frh), and fine-grained sandstones (Sm) (Fig. 6). The mudstone and siltstone beds are characterized by planar-parallel lamination in tabular 0.05–0.5 m thick beds (Fig. 4h). These mudstone facies are interbedded with tabular, laterally continuous beds of fine-grained white to yellowish massive sandstones (Sm).

Two petrography samples were collected in the facies Sm, which are characterized by 30 and 42% of a ferruginous and sparitic cements (Fig. 5c). These samples are well sorted and dominated by well-rounded to sub-rounded grains (Table 3). The grains are mostly monocrystalline and polycrystalline quartz with minor amounts of feldspars. These samples plot in the craton interior field in the tectonic discrimination diagram of Dickinson (1985) (Fig. 5a).

The association of facies Fgh, Frh, and Sm indicate deposition by combined processes of decantation and tractive currents in subaqueous conditions. We interpret this association to represent a fresh lake setting with sporadic underflow currents (Anadon et al., 1991; Bridge and Demicco, 2008).

4.3. Upper Río Salí Fm

This unit conformably overlies the Middle Río Salí Fm. It was described in sections 5 and 7, in the central part of the Choromoro basin (Fig. 2). This unit is composed of the facies assemblages (V) in the basal section and (IV) towards the top. Facies assemblage (V) is mainly composed of gypsum (Y) and red to brown mudstones and siltstones, with abundant gypsum nodules and disseminated crystals (Fy) (Table 1). Gypsum and mudstone beds are characterized by parallel to undulatory lamination. These facies are presented in tabular and laterally continuous beds between 0.1 and 1.4 m-thick.

The abundance of primary gypsum suggests that this facies assemblage was deposited in an inner saline lake system. Facies Fy is interpreted as saline mudflats, and the facies (Y) are characteristic of saline lake pans (Nichols, 2009).

4.4. Lower India Muerta Fm

This unit was described in the Choromoro and Tucuman basins (sections 5 and 10, Fig. 2). It overlies the upper Río Salí Fm. with a para-conformable sharp contact (Fig. 5a). The Lower India Muerta Fm. is characterized by the facies assemblage (VI), which is mainly composed of fine-grained to coarse-grained sandstones (Sh and Sm) interbedded with brown siltstones (Frh). Facies Sh corresponds to thin layers (< 0.1 m) of fine to medium-grained sandstones with horizontal laminations and frequent convoluted laminations, organized in 1–2 m-thick tabular stacked packages (Fig. 4d). Facies Sm corresponds to massive medium to coarse-grained sandstones in 1–5 m-thick tabular beds with well-defined planar contacts. Sandy facies are interbedded with 1–3 m-thick siltstone beds (Frh), displaying distinctive sedimentary couplets.

Six sandstone petrography samples collected in the facies Sm and Sh are characterized by 20–42% of a clay-rich matrix and sparitic cement. These samples are composed of well-sorted, sub-angular grains of monocrystalline and polycrystalline quartz, alkaline feldspar and plagioclase, and lithics. Lithic grains are metamorphic micaceous

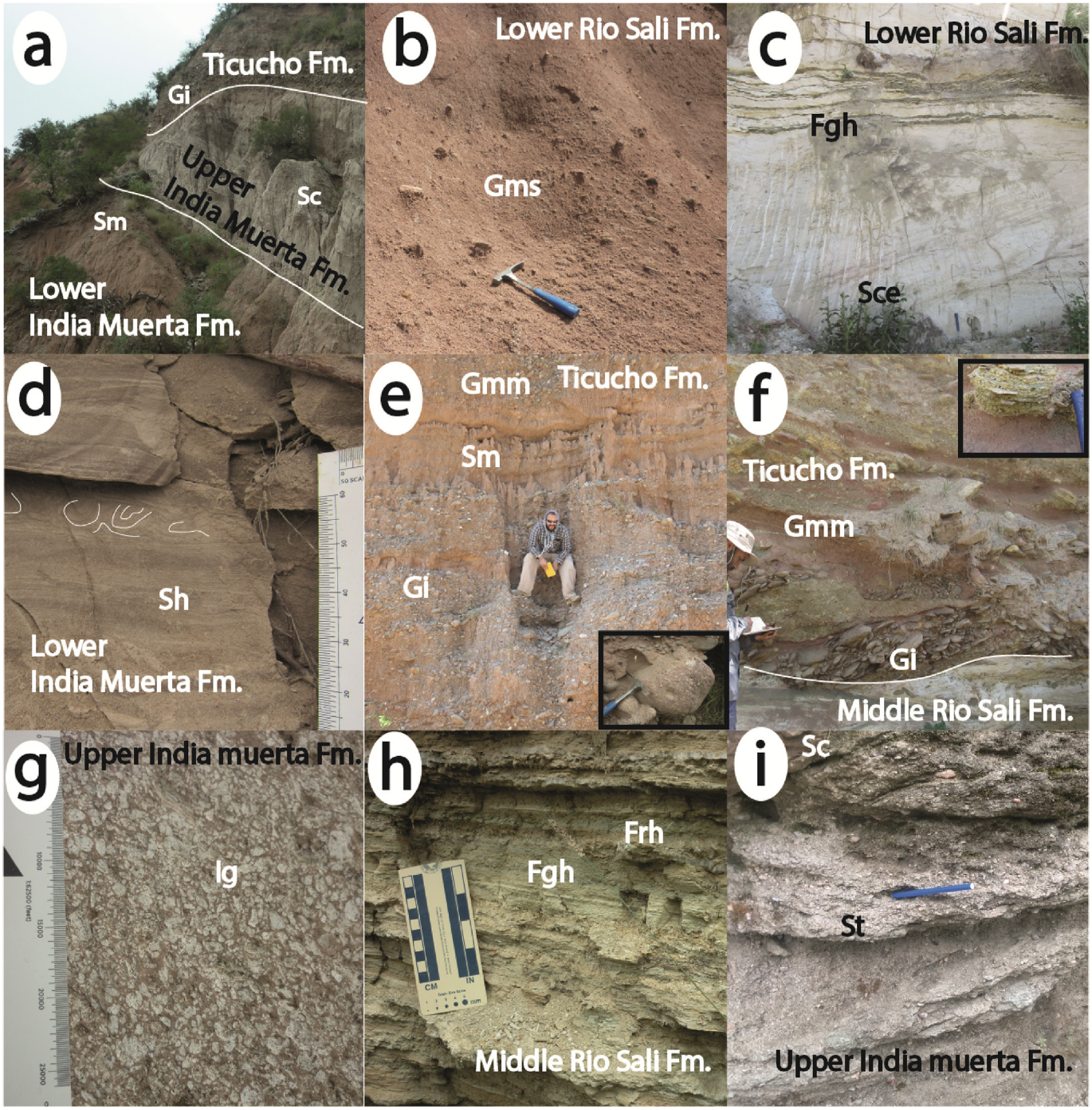

Fig. 4. Field photos of the more distinctive sedimentary facies in the Choromoro and Tucuman basins. In Fig. 4e, a distinctive sedimentary clast from the Cretaceous syn-rift strata is shown in the inset black square. In Fig. 4f, the black square shows a clast from the Middle Río Salí Fm. in the Ticucho Fm.

fragments and ferruginous fine-grained siltstones (Fig. 5d). These samples plot in the recycled orogeny field in the tectonic discrimination diagram of Dickinson (1985) (Fig. 5a).

Facies association (VI) is interpreted as the result of high energy unconfined sheet floods in a terminal alluvial fan or an ephemeral fluvial system. This interpretation is based on sheet-like laterally continuous geometries, and the characteristic sedimentary couplets between the high energy rapid deposited sandy flows (Sm and Sh) and the fine-grained overbank suspension deposits (Frh) (Miall, 2013; Sohn, 1997).

4.5. Upper India Muerta Fm

This unit was described in the Tucuman and the Choromoro basins (Section 7, Figs. 2 and 5). It is characterized by the presence of facies assemblages (VII) and (VIII) (Table 2). Facies (VII) is mainly composed of coarse-grained sandstones and pebbly conglomerates (Gt, St, Sc, and Gc) (Fig. 4i). Coarse-grained sandstones and pebbly conglomerates have planar and trough cross-bedding. This facies is characterized by 1–3 m lenticular beds, which laterally transition to massive conglomeratic sandstones (Sm). One petrographic sample collected in facies Sm has 28% of sparitic cement, a similar composition compared to the Lower India Muerta Fm.; both plot in the recycled orogen field on the tectonic

Table 3
Petrography and clast counts results.

		Río Salí Fm.				India Muerta Fm.					
		16140RN	16115GZ	16120GZ	16116GZ	16127IM	16052PV	17173IM	17174IM	17178AC	17176AC
Qt	Qmr (%)	10	5	12	11	1	5	3	18	3	6
	Qmo (%)	68	51	54	57	49	47	46	33	47	48
	Qpr (%)	2	1	1	3	3	0	2	14	2	0
	Qpo (%)	4	8	6	1	1	8	1	7	1	3
F	Fk (%)	11	2	13	15	9	8	9	8	10	5
	Mic (%)	0	0	5	4	0	0	1	1	0	0
	Pl (%)	4	2	10	8	3	3	5	5	10	3
L	Ls (%)	0	0	0	0	6	14	9	8	4	4
	Lm (%)	0	2	1	1	0	0	2	5	1	1
Others	Hb (%)	0	1	0	0	0	0	1	0	1	0
	Op (%)	0	7	0	0	4	3	2	0	1	4
	Bt (%)	0	10	0	0	15	3	11	1	13	19
	Mcs (%)	1	10	0	0	8	7	7	0	8	7
Matrix and cement	M (%)	0	15	0	0	6	18	21	1	18	19
	Cf (%)	0	15	0	0	0	0	0	0	0	0
	Cm (%)	31	0	3	3	0	0	0	4	0	0
	Cs (%)	11	0	33	26	29	0	0	23	0	0
Totals	TG	300	307	303	300	304	300	336	353	317	317
	TC	516	438	472	422	466	365	427	485	387	392
Clast counts											
			Vc	**Mt**	**Pl**	**Qz**	**Sd**	**Tf**	**Tt**		
Upper India Muerta Fm.			12	0	32	0	0	56	100		
Ticucho Fm.			0	72	7	10	11	0	100		

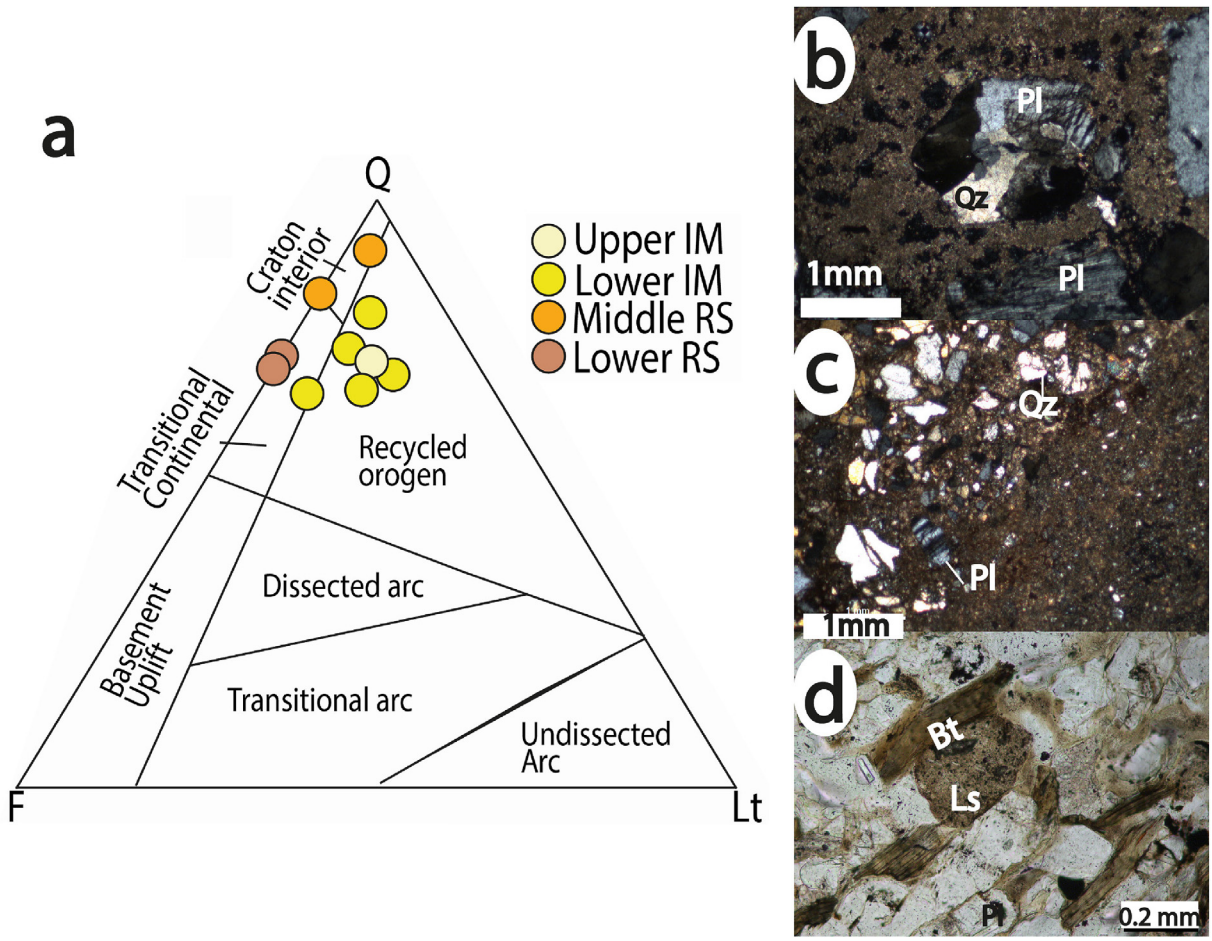

Fig. 5. (a) QFLt plot from Dickinson (1985). (b) Polarized thin section photograph from the Lower Río Salí Fm. Pl: plagioclase and Qz: monocrystalline quartz. (c) Polarized thin section photograph from the Middle Río Salí Fm. (d) Thin section photograph from the Lower India Muerta Fm. Ls: sedimentary lithic and Bt: biotite.

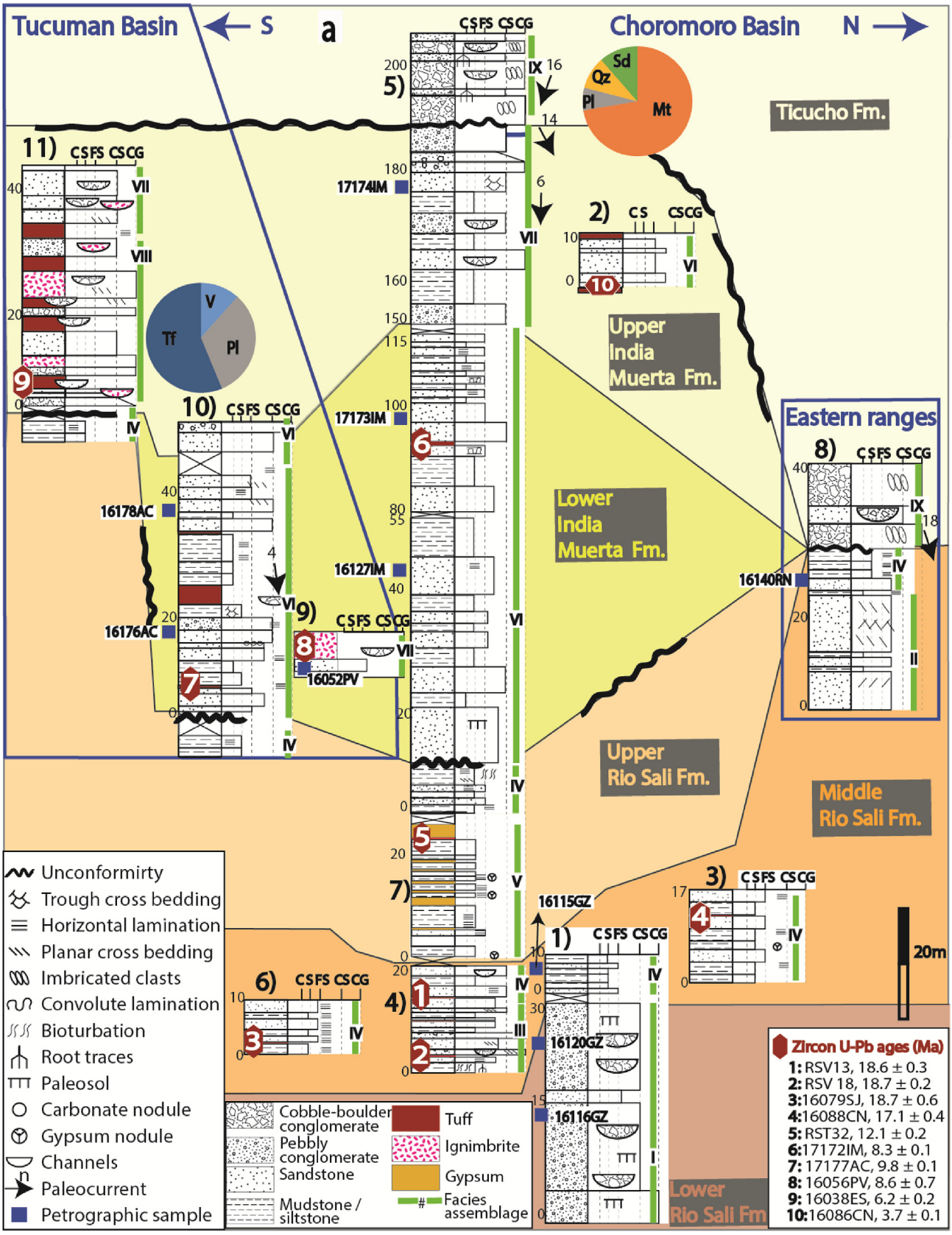

Fig. 6. Stratigraphic sections in the Choromoro and the Tucuman basins. The sections are arranged from the south (left) to the north (right), except section 8, which is located to the east of the Choromoro basin. Blue lines denote basin boundaries; locations of the sections are presented in Fig. 2. The background colors represent the different stratigraphic units. Red polygons with white number represent the U-Pb ages presented in the key; ages are described in detail in section 5. Petrographic samples are represented by the blue squares. Rounded pies represent the clast count results. Qz: milky quartz, Sd: sedimentary lithics, Pl: Plutonic lithics, Tf: tuff lithics, and Mt: metamorphic lithics. (For interpretation of the references to color in this figure legend, the reader is referred to the Web version of this article.)

discrimination diagram of Dickinson (1985) (Fig. 5a).

Facies assemblage (VII) is interpreted as the result of bedload transport and accumulation of coarse-grained clastic material in a braided fluvial depositional system. This interpretation is based on the fluvial architectural elements, such as channels and fluvial bars, and the tractive structures observed in these channel fills system (Miall, 2013; Nichols, 2009).

Facies assemblage (VIII) is represented by to 1–3 m thick beds of ignimbrites (Ig), ashes (T), and conglomerate (Gmv). Ignimbrite (Ig) beds are composed of poorly sorted pumiceous clasts; these are occasionally welded (Fig. 4g). These ignimbrite beds are discontinuous and have lenticular geometries. Fine-grained ashes (T) are presented in continuous tabular beds with planar contacts and interbedded with the facies (Ig). Facies Gmv is composed of a matrix-supported massive conglomerate with abundant pyroclastic material such as pumice pebbles (56%) and a crystal-rich matrix. Facies Gmv also includes volcanic (12%) and plutonic pebbles (32%) (Table 3) (Fig. 6).

Facies VIII is interpreted as the result of volcanoclastic and pyroclastic deposition proximal to a volcanic center. The couplets of facies (Ig) and (T) are characteristic of pyroclastic high-density flows, which normally occur tens of kilometers from the volcanic center (Orton, 1995). Facies Gmv is interpreted as the result of debris flows responsible for reworking and re-depositing primary pyroclastic material (Orton, 1995).

Qmr: Monocrystalline quartz with non-undulatory extinction, Qmo: Monocrystalline quartz with undulatory extinction, Qpr: Polycrystalline quartz with non-undulatory extinction, QPo: Polycrystalline quartz with undulatory extinction, Fk: alkaline feldspar, Mic: microcline, Pl: plagioclase, Ls: sedimentary lithics, Lm: metamorphic lithics, Hb: hornblende, Op: opaque, Mcs: muscovite, M: matrix, Cf: ferruginous cement, Cm: micritic cement, Cs: sparitic cement, TG: total counted grains, TC: total counted points, Vc: volcanic clast, Mt: Metamorphic clast, Pl: plutonic clasts, Sd: sedimentary clast, Tf: tuff clast, Tt: counted clasts. Sample locations are presented in Fig. 6.

4.6. Ticucho Fm

This unit was recognized in the Choromoro basin overlaying the Upper India Muerta Fm. and the Lower Río Salí Fm. (Section 5 and 8, Figs. 2 and 5a). The lower limit of this unit corresponds to a pronounced erosional angular unconformity (Fig. 4a and f). This unit is composed of the facies assemblage (IX), which is mainly composed of cobble to boulder conglomerates and subordinate beds of coarse-grained sandstones (Sm). Coarse-grained clast-supported conglomerates are imbricated (Gi) in 1.5–4 m thick discontinuous lenticular beds. Facies Gi is associated with reddish sandstone massive beds (Sm), presented in tabular continuous beds. Facies Gi is composed of metamorphic (72%), igneous (7%), quartz (10%), and sedimentary pebbles (11%) (Fig. 6).

Facies Sm is also characterized by the presence of root traces and iron-rich paleosols. These strata are interbedded with levels of poorly sorted matrix supported angular to subangular cobble to boulder conglomerates (Gmd), presented in discontinuous lenticular beds.

The facies assemblage (IX) is interpreted to result from different depositional processes in a proximal fluvial system. Fluvial bed forms defining cobble to boulder conglomerates (Gi) suggest bedload transport and accumulation in channel system proximal to a high relief source area. Paleosols were developed in sandy floodplains formed on overbank deposition (Miall, 2013). Finally, facies Gmd is the result of proximal debris flows within fluvial valleys (Mulder, 2011).

5. U-Pb ICPMS geochronology results

We analyzed ten pyroclastic rocks interbedded with the described stratigraphic units. We present seven U-Pb LA-ICP-MS ages interpreted as depositional volcanic tuff ages and three interpreted as maximum depositional ages (Fig. 7) (Table 4). In the Choromoro basin, four ages were obtained from samples collected in centimetric layers of fine-grained tuffs of the Middle Río Salí Fm. Two of these samples (RSV 13 and RSV 18) exhibit overlapping ages of 18.6 ± 0.3 and 18.7 ± 0.2 Ma, respectively (Fig. 7). Moreover, similar maximum depositional ages of 18.7 ± 0.3 and 17.1 ± 0.4 Ma were obtained from samples 16079SJ and 16088CN, in sections 3 and 6 (Figs. 2 and 5). The sample RST 32, collected in a discontinuous tuff bed in the Upper Río Salí Fm. (section 7), yielded an age of 12.1 ± 0.2 Ma.

In the Choromoro basin, an age of 8.3 ± 0.1 Ma was obtained from a 10 cm thick tuff (Sample 17172IM) in the Lower India Muerta Fm. In the Tucuman Basin, ages of 9.8 ± 0.1 (17177AC) and 8.6 ± 0.7 Ma (16056 PV) were obtained from ~1 m thick tuff beds. These ages were obtained in outcrops previously mapped as the Aconquija Fm. Based on these new ages, we attribute this strata to the Lower India Muerta Fm. Sample 16038 ES from the unit described here as the Upper India Muerta Fm. and previously mapped as the Aconquija Fm. yielded an age of 6.2 ± 0.2 Ma. Sample 16086CN was collected in the Upper India Muerta Fm. and yielded a maximum depositional age of 3.7 ± 0.1 Ma (Figs. 5 and 6).

6. Stratigraphic correlation of the sedimentary units in the Choromoro and the Tucuman Basins

Lacustrine facies of the Middle Río Salí Fm. yield volcanic tuff ages and maximum depositional ages around ~18 Ma (Fig. 7). This fresh-water lacustrine interval represents a reliable correlation level between the Choromoro and Tucumán basins (Fig. 6). The Lower Río Salí Fm. was unconformably deposited on top of the Paleocene-Early Eocene Rio Loro Fm. As the Lower Río Salí Fm. is stratigraphically below the Middle Río Salí Fm., the age is constrained to lie between the Early Eocene and Early Miocene (~18 Ma). The depositional system changed from the fresh-water lacustrine environment described in the Middle Río Salí Fm. towards a more saline and restricted lacustrine system in the Upper Río Salí Fm. These saline facies are mostly preserved in the center of the Choromoro basin and southwest of the Guasayan range (Dal Molin et al., 2003; Gavriloff and Bossi, 1992). The ages obtained from the Middle and Upper Río Salí formations suggest that this environmental transition took place between ~18 and 12 Ma.

The Lower India Muerta Fm. was paraconformable deposited on top of the Upper Río Salí Fm. This unit is characterized by a change from saline lacustrine to ephemeral fluvial deposits between ~11 and 8 Ma. This unit is well preserved in the center of the Choromoro basin (Fig. 2). In the Tucuman basin, the units previously mapped as the Eocene Aconquija Fm. (Dal Molin et al., 2003) exhibit similar facies and similar U-Pb ages compared to the Lower India Muerta Fm.; therefore, we consider these to be the same unit. The Upper India Muerta Fm. is characterized by deposition in a more permanent fluvial system; this transition was also described in sections 5 and 10 and dated as ~6 Ma in section 11 (Figs. 2 and 6). In section 2 (Fig. 2), facies correlatable with the Upper India Muerta Fm. yield maximum depositional ages of ~3 Ma, representing the youngest record of this unit. The Ticucho Fm. was deposited on top of a pronounced erosional unconformity identified in both basins. Based on previous work this unit is considered to be younger than ~3 Ma (Georgieff et al., 2014).

7. Paleogeography and stratigraphic correlations

7.1. Stage 1: a continuous Miocene foreland basin (30? - 13 Ma)

Previous studies have considered the lacustrine record of the Río Salí Fm. (~18–12 Ma) to be coeval with the lacustrine episodes in the surrounding basins (e.g. Santa Maria and Metan basins). In these basins, the lacustrine deposits yield ages between ~14 and 10 Ma, contemporaneous with the Paranaense marine transgression (15–6 Ma) (Fig. 9) (e.g. Gavriloff and Bossi, 1992; Lovejoy et al., 2006; Ruskin

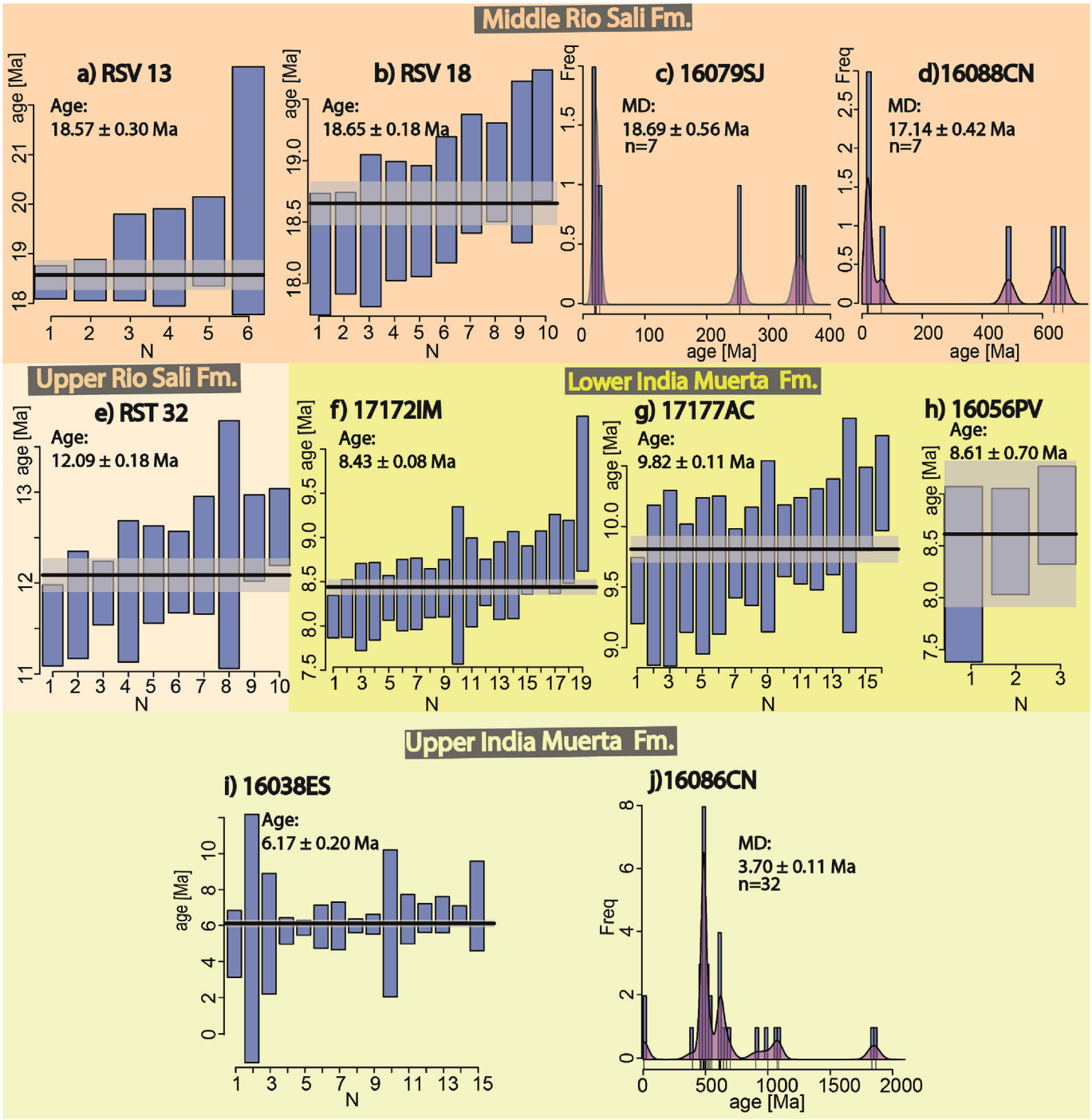

Fig. 7. U-Pb LA ICP-MS weighted average and maximum depositional (MD) zircon ages from samples collected in the Miocene units of the Choromoro and the Tucuman basins. Background colors denote the unit where the sample was collected. Single grain ages are presented in Table S1. The details of the age calculation are presented in section 3.3. (For interpretation of the references to color in this figure legend, the reader is referred to the Web version of this article.)

et al., 2011). However, our results suggest that the transgressive lacustrine system preserved in the Choromoro and Tucuman basins started around ~18 Ma and is older than the lacustrine strata deposited in the Santa Maria basin (Fig. 8). The onset of Miocene sedimentation in the Choromoro and Tucuman basins occurred prior to the onset in the Santa Maria basin; this may suggest that the Choromoro and the Tucuman basins were situated at a slightly lower elevation than the surrounding basins during the onset of Miocene deposition.

Based on thermal modeling of AHe and AFT data, Zapata et al. (2018) proposed the existence of a Paleogene broken foreland in the study area; at this time, several basement blocks formed positive relief elements. The coarse-grained proximal facies described as the Lower Río Salí Fm. in the Choromoro basin may be the sedimentary expression of the erosion of these preserved topographic elements during Oligocene or the Early Miocene (> 18 Ma) (Fig. 8a) (Gavriloff and Bossi, 1992). However, more temporal constraints are required for this unit. During the Miocene, increased basin subsidence due to the eastward propagation of the orogenic wedge (Löbens et al., 2013; Mortimer et al., 2007) facilitated deposition of the sediments of the Middle Río Salí Fm. These lacustrine facies were deposited on top of the basement and on top of the Paleogene units, filling up the remnants of the Eocene topography.

Table 4
ICPMS U-Pb ages.

Sample	Unit	Latitude	Longitude	Age (Ma)	2σ error	MSWD	Age grains	Analyzed Grains	type
RSV13	Middle Río Salí	−26.498	−65.4064	*18.57*	*0.26*	*1.2*	*6*	15	Volcanic age
RSV18	Middle Río Salí	−26.498	−65.4064	*18.65*	*0.2*	*1.58*	*10*	22	Volcanic age
16079SJ	Middle Río Salí	−26.633	−65.3744	*18.69*	*0.56*	-	*1*	9	detrital (MD)
16088CN	Middle Río Salí	−26.129	−65.0803	*17.14*	*0.42*	-	*1*	32	detrital (MD)
RST 32	Upper Río Salí	−26.596	−65.2846	*12.1*	*0.18*	*2.01*	*10*	27	Volcanic age
17172IM	Lower India Muerta	−26.549	−65.2709	*8.43*	*0.08*	*1.75*	*19*	27	Volcanic age
17177AC	Lower India Muerta	−27.323	−65.9123	*9.81*	*0.11*	*1.12*	*16*	32	Volcanic age
16056 PV	Lower India Muerta	−27.146	−65.7509	*8.62*	*0.7*	*0.72*	*3*	12	Volcanic age
16038 ES	Upper India Muerta	−27.64	−65.7917	*6.17*	*0.2*	*1.85*	*15*	20	Volcanic age
16086CN	Upper India Muerta	−26.124	−65.1167	*3.7*	*0.11*	-	*1*	32	detrital (MD)

An extended foreland basin developed after the residual Paleogene relief was completely fill-up (Fig. 9b). The blocks in relatively low relief positions were reheated; higher relief elements were probably covered, but the thickness of the sedimentary cover was not enough to partially reset the apatite (U-Th-Sm)/He system there (Zapata et al., 2018). During this period, the Peñas Azules Fm. was deposited in the Cajon basin in a fluvial system characterized by eastward-directed paleoflows (Fig. 9) (Mortimer et al., 2007; Pratt et al., 2008). Immediately east of the Cajon basin, a freshwater lacustrine system developed in the Santa Maria and Choromoro basins; thus it is plausible that the fluvial system was connected to this continuous lacustrine system, as other authors have also suggested (Fig. 9b) (Mortimer et al., 2007; Pratt et al., 2008).

7.2. Stage 2: the onset of deformation and basin fragmentation (13–6 Ma)

Between ~18 and 12 Ma, the lacustrine depositional system changed from a freshwater lake system in the Middle Río Salí Fm. towards a saline lake system recorded in the Upper Río Salí Fm. Conversely, in the Santa Maria basin, the San Jose Fm. represents freshwater lake facies (Gavriloff and Bossi, 1992; Georgieff et al., 2014; Ruskin et al., 2011) concomitant with the Upper Río Salí saline lake (Fig. 8). Exhumation between 13 and 10 Ma has been documented north of the Tucuman Massif and in the Aconquija range (Fig. 2) (Zapata et al., 2018). During the onset of basin inversion, deformation formed relatively low elevation barriers in the Aconquija range and the Tucuman massif; these barriers were sufficient to reorganize the drainage system and to fragment the former lacustrine basin (Figs. 8 and 9c). The separation of the Tucuman and the Choromoro basins from the fluvial systems coming from the west may have isolated the lake system, reducing the supply of fresh water and sediments in the Choromoro and the Tucuman basins; these conditions favor the development of a restricted saline lake system (Fig. 9c). The increase of global temperatures during the Middle Miocene (~15 Ma) climate optimum (Mudelsee et al., 2014) may have facilitated water evaporation, and thus the formation of this saline lake system. The transition to saline lacustrine depositional settings and basement exhumation and deformation mark the onset of the fragmentation of the former foreland basin.

Between 10 and 6 Ma, most of the basins were characterized by the deposition of fine-grained unconfined sheetfloods in an ephemeral fluvial system (Fig. 7) (Bossi and Muruaga, 2009; Mortimer et al., 2007; Spagnuolo et al., 2015). In the Tucuman and Choromoro basins, these depositional conditions characterized the Lower India Muerta Fm., which is paraconformably deposited on top of the Middle and the Upper Río Salí Fm., marking the end of the lacustrine system. The sandstones of the Lower India Muerta Fm. are characterized by hyper-concentrated gravitational flows and the presence of fine-grained ferruginous sedimentary lithics (Fig. 5a). The sedimentary lithics and the immature and high energy character of the Lower India Fm. can be interpreted as a result of the reworking of poorly cemented Miocene and Paleogene sedimentary cover. The fast removal of the highly erodible sedimentary deposits prevented significant surface uplift within the basins (Fig. 9d). The transition from lacustrine to fluvial ephemeral depositional setting was the result of the reworking of the sedimentary cover during the fragmentation of the foreland basin.

Between 12 and 5 Ma, the Farallon Negro and the Agua Rica volcanic complexes were emplaced in the Campo-Arenal basin and in the southern part of the Aconquija range, respectively (Harris et al., 2004; Landtwing et al., 2002). We described and dated two tuffs associated with high-density pyroclastic flows on the eastern flank of the Aconquija range and on top of the Ambato range (Sections 9 and 11 in Figs. 2 and 5). These tuffs yielded ages of 6.2 ± 0.2 and 8.6 ± 0.2 Ma (Fig. 7), correlatable with the ages of the Farallon Negro and the Agua Rica volcanic and plutonic rocks, respectively (Fig. 8). High-density pyroclastic flows typically do not travel more than a few tens of kilometers (e.g. Druitt and Sparks, 1982; Fisher and Schmincke, 2012). Moreover, the volcano-sedimentary record of the Farallon Negro complex does not include high-density pyroclastic material. Therefore, one plausible explanation is that these flows were most likely related to the more proximal Agua Rica complex (Fig. 2). This assumption implies that after initial exhumation, a volcanic complex developed in the southern Aconquija range in a relatively high elevation position (Fig. 8d). This volcanic structure was subsequently eroded after 5 Ma. The ignimbrite flows preserved in an intermountain basin on top of the Ambato range imply that this basement block remained in a relatively low relief position until ~6 Ma (Fig. 9e).

7.3. Stage 3: relief development and basin compartmentalization (6–0 Ma)

After 6 Ma, in all the basins, the depositional conditions changed from ephemeral fluvial systems to well-defined permanent fluvial systems (Fig. 8). This change was facilitated by the development of significant relief in the surrounding ranges. After the initial removal of the poorly cemented, young sedimentary cover, the exposure of more resistant crystalline basement leads to less efficient erosion (Flowers and Ehlers, 2018; Sobel et al., 2003), resulting in an increase of relief. Less efficient basement erosion is also apparent in the preservation of old planation surfaces on top of the Quilmes, Hualfin, Cumbres Calchaquies, and Ambato ranges. The paleocurrents in the Cajon and the Villavil basins suggest that this fluvial system flowed towards the SE (Bossi and Muruaga, 2009; Pratt et al., 2008). Therefore, we consider that the Campo-Arenal and Pipanaco basins were connected and that the Capillitas range did not constitute a barrier between 6 and 3 Ma (Fig. 9d).

After 3 Ma, boulder conglomerates of the Punaschotter were unconformably deposited on top of the proximal fluvial units in the intermountain basins west of the Aconquija range (Fig. 8). This change in the depositional system was related to the development of the orographic barriers responsible for creating a more closed drainage system and the aridification of these basins, as other authors have also suggested (Mortimer et al., 2007; Schoenbohm et al., 2015). Farther east, after 3 Ma, proximal fluvial facies of the Ticucho Fm. were

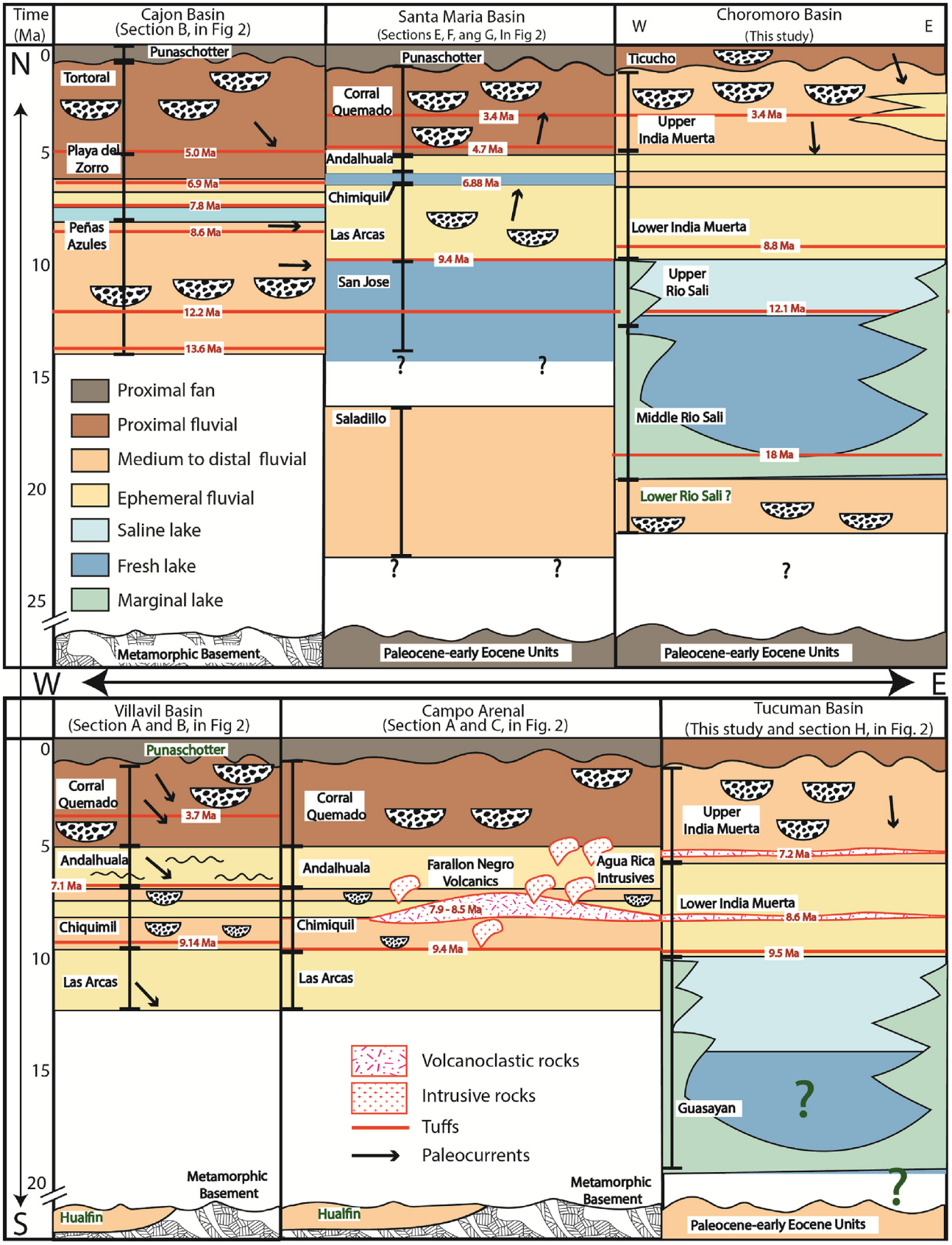

Fig. 8. Chronostratigraphic chart of the Choromoro and the Tucuman foreland basins and high-elevation intermountain basins located to the west. The locations of the sections and the references used in this compilation are presented in Fig. 2. Colors denote simplified depositional environments, red lines represent the available tuff ages and the black arrows denote paleocurrent directions. (For interpretation of the references to color in this figure legend, the reader is referred to the Web version of this article.)

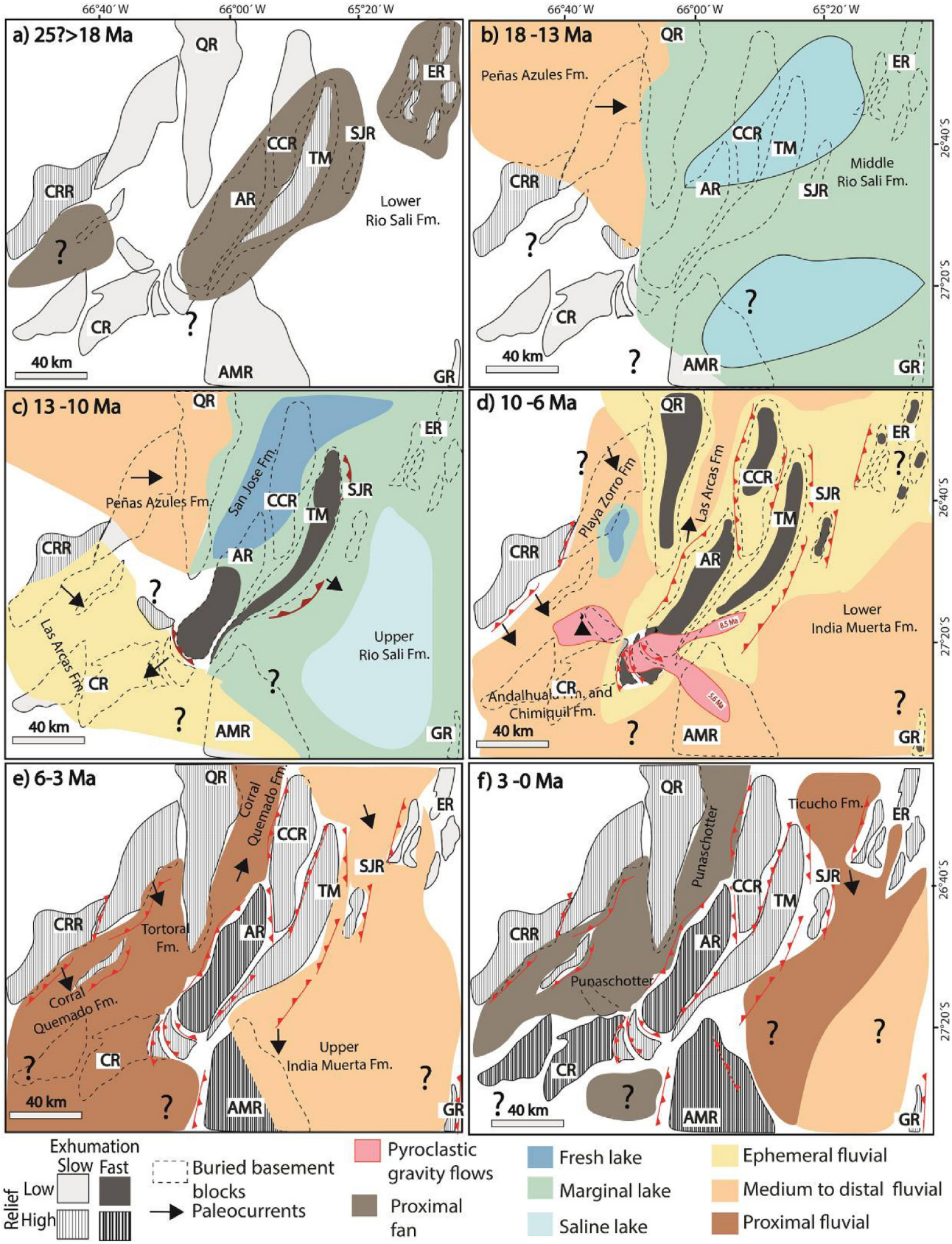

Fig. 9. Schematic time-dependent evolution of the Andean retroarc between 26 and 28°S. CR: Chango Real range, QR: Quilmes range, TM: Tucuman massif, CCR: Cumbres Calchaquies range, SJR: San Javier range, CHR: Cuevas-Hualfin range, CP: Capillitas range, AR: Aconquija range, TVR: Tafi del Valle range, AMR: Ambato range, ER: Eastern ranges GR: Guasayan range.

unconformably deposited on top of the folded Río Salí and India Muerta formations (Fig. 4e and F). This basin-scale unconformity is related to the development of relief in the eastern ranges and to the development of the Aconquija and Cumbres Calchaquies orographic barriers, which enhanced erosion and precipitation on the humid foreland side. This interpretation is based on the proximal debris flows, paleocurrents in proximal fluvial settings, and the presence of local sedimentary sources, indicated by sedimentary clasts from Cretaceous syn-rift deposits and the middle Río Salí Fm.

8. Landscape response to interactions between tectonics, climate, and rock erodability

Our results, combined with the abundant stratigraphic, geochronologic, and thermochronologic data in the study area, offer an opportunity to perform a detailed source to sink analysis. Linking the uplift and exhumation history of the ranges with the depositional record allows us to understand linkages between tectonics, climate, and rock erodability. As a result, we are able to distinguish three main stages in the evolution of relief and the depositional systems in the study area.

In the first stage, the tectonically-controlled increase of accommodation space allowed fine-grained strata to fill up the preexisting topography, reduced the relatively low relief, and formed a continuous foreland basin. The onlapping character of the fine-grained strata and differential basement reheating are the records of relief reduction due to the incorporation of preexisting positive relief elements into the foreland basin (e.g. DeCelles and Giles, 1996; Gupta and Allen, 2000). Since the paleo-topographic record can be obscured during subsequent deformation phases, these sedimentation patterns and the thermal history of the basement blocks can help to understand the reduction of older relief.

Stage two is characterized by the onset of tectonically controlled unroofing of the former basin due to the forelandward propagation of deformation and the cannibalization of the former foreland basin. This phase is characterized by rapid exhumation due to the removal of the easily eroded young sedimentary cover. As a consequence of efficient erosion, no significant relief was developed in this time (e.g. Flowers and Ehlers, 2018; Sobel and Strecker, 2003; Whipple and Tucker, 1999). The incipient low relief formed during the early stages of basin unroofing was enough to change the drainage system and to compartmentalize the former foreland basin. The reworking of fine-grained sediments in a low relief facilitated the development of an ephemeral fluvial system, characterized by proximal sandy alluvial fans. We have documented how local changes in the foreland lacustrine system and the development of ephemeral fluvial systems are the records of initial rapid basement exhumation, basin unroofing, and limited relief development.

In the third stage, the exposure of crystalline basement with low erodability slowed down basement exhumation and caused surface uplift (e.g. England and Molnar, 1991; Flowers and Ehlers, 2018; Sobel et al., 2003; Whipple and Tucker, 1999). The development of relief caused the formation of well-defined valleys and associated stable fluvial systems. Prolonged surface uplift eventually modified atmospheric circulation, forming an orographic barrier. This changed the local climates, reducing the erosion rates on the arid side, and increasing erosion and thus exhumation on the humid side (Bookhagen and Strecker, 2012; Hilley and Coutand, 2010; Kleinert and Strecker, 2001; Roe et al., 2008; Sobel and Strecker, 2003). After the development of the rain shadow, the dry side was characterized by the storage of proximal gravitational flows as a result of basin aridification and a more closed drainage system (Schoenbohm et al., 2015). In contrast, the increased water supply facilitated the development of proximal open fluvial systems on the humid side.

These stages record how the onset of tectonically-driven exhumation and deformation do not coincide with the development of relief. The stratigraphic marker for the onset of basin fragmentation was the change in lacustrine conditions followed by the transition towards an ephemeral fluvial depositional system. The subsequent transition from an ephemeral to a permanent fluvial system records the development of relief in the study area. Finally, the pronounced erosional unconformities and a change to gravitational alluvial sedimentation on the dry side records the development of the orographic barriers (Flowers and Ehlers, 2018; Roe et al., 2008; Schoenbohm et al., 2015; Sobel and Strecker, 2003; Willett, 1999). Clearly, the relationships between tectonics, climate, and rock erodibility discussed here are critical for the interpretation of sedimentation, deformation, and exhumation patterns during mountain building.

9. Conclusions

We have documented the Miocene stratigraphic evolution of the Choromoro and Tucuman foreland basins. During the Early Miocene (~18 Ma), lacustrine sediment filled up the preexisting Paleogene topography, reheated several basement blocks, and formed a continuous foreland basin. During the Middle and the Late Miocene (~15-6 Ma), the eastward progression of deformation fragmented the former foreland basin. Initial basin unroofing was characterized by low relief, basin fragmentation, and the development of an ephemeral fluvial system. After the removal of the sedimentary cover; the low erodibility of the crystalline basement facilitated the increase of relief and the formation of orographic barriers on the western margin of the basins. This increase in relief brought more moisture into the basin, thereby shifting the depositional system towards a more permanent proximal fluvial system. Our findings highlight the response of depositional systems during basin subsidence, foreland basin fragmentation, and topographic growth.

Data availability

All the data used in this manuscript can be found in the supporting information (Table S1).

Acknowledgments

We acknowledge the Deutsche Forschungsgemeinschaft (DFG, grant STR 373/34-1) and the Brandenburg Ministry of Sciences, Research and Cultural Affairs, Germany for funding this study as part of the International Research Training Group IGK2018 (StRATEGy). We also acknowledge the German-Argentine University Network (DAHZ/CUAA), the Argentinean science foundation (CONICET and PICT 1274), and CICTERRA, for their funding and support on the basis of a joint Cotutelle-de-thèse. ERS and RZ thank the DAAD and Universities Australian for funding by the Australia-Germany Joint Research Cooperation Scheme. We would especially like to thank M. Strecker and I. Petrinovic for helpful discussions, and A. Bergner, H. Wichura, V. Torres, and A. Gutierrez for their administrative support.

Appendix A. Supplementary data

Supplementary data to this article can be found online at https://doi.org/10.1016/j.jsames.2019.102238.

References

Coughlin, T.J., O'Sullivan, P.B., Kohn, B.P., Holcombe, R.J., 1999. Apatite fission track thermochronology of Sierras Pampeanas central western Argentina: implications for the mechanism of plateau-uplift in the Andes. Geology 26 (11), 999–1002. https://doi.org/10.1130/0091-7613(1998)026<0999:AFTTOT>2.3.CO;2.

England, P., Molnar, P., 1990. Surface uplift, uplift of rocks, and exhumation of rocks. Geology 18 (12), 1173–1177. https://doi.org/10.1130/0091-7613(1990)018<1173:SUUORA>2.3.CO;2.

Horton, B.K., DeCelles, P.G., 1997. The modern foreland basin system adjacent to the

Central Andes. Geology 25 (10), 895–898. https://doi.org/10.1130/0091-7613(1997)025<0895:TMFBSA>2.3.CO;2.
Allen, P.A., 2008. From landscapes into geological history. Nature 451, 274. Retrieved from. https://doi.org/10.1038/nature06586.
Anadon, P., Cabrera, L., Kelts, K., 1991. Lacustrine Facies Analysis. International Association of Sedimentologists (IAS) Special Publication No. 13. Blackwell Scientific Publications, Oxford.
Black, L.P., Kamo, S.L., Allen, C.M., Davis, D.W., Aleinikoff, J.N., Valley, J.W., et al., 2004. Improved 206Pb/238U microprobe geochronology by the monitoring of a trace-element-related matrix effect; SHRIMP, ID–TIMS, ELA–ICP–MS and oxygen isotope documentation for a series of zircon standards. Chem. Geol. 205 (1–2), 115–140.
Blair, T.C., McPherson, J.G., 2009. Processes and Forms of Alluvial Fans. Geomorphology of Desert Environments. https://doi.org/10.1007/978-1-4020-5719-9_14.
Bonini, R.A., Georgieff, S.M., Candela, A.M., 2017. Stratigraphy, geochronology, and paleoenvironments of Miocene - Pliocene boundary of san Fernando, Belén (Catamarca, northwest of Argentina). J. South Am. Earth Sci. 79, 459–471. https://doi.org/10.1016/j.jsames.2017.08.020.
Bookhagen, B., Strecker, M.R., 2012. Spatiotemporal trends in erosion rates across a pronounced rainfall gradient: examples from the southern Central Andes. Earth Planet. Sci. Lett. 327, 97–110. https://doi.org/10.1016/j.epsl.2012.02.005.
Bossi, G.E., 1969. Geología y estratigrafía del sector sur del Valle de Choromoro. Universidad Nacional de Tucumán, Fundación e Instituto Miguel Lillo.
Bossi, G.E., Muruaga, C.M., 2009. Estratigrafía inversión tectonica del “rift” Neogeno en el Campo del Arenal, Catamarca, NO Argentina. Andean Geol. 36 (2), 311–341. https://doi.org/10.4067/S0718-71062009000200007.
Bossi, G.E., Palma, R., 1982. Reconsideración de la estratigrafía del valle de Santa María, provincia de Catamarca, Argentina. In: Congreso Latinoamericano de Geología, vol. 5. pp. 155–172.
Bossi, G.E., Gavriloff, I.J.C., Esteban, G., 1998. In: Gianfransisco, M., Puchulu, M.E., Durango de Cabrera y GF Aceñolaza, J. (Eds.), Terciario, estratigrafía, bioestratigrafía y paleogeografía. *Geología de Tucumán., Publicación Especial.* Colegio de Graduados de Ciencias Geológicas de Tucumán, Tucumán, pp. 87–108.
Bossi, G.E., Georgieff, S.M., Gavriloff, I.J.C., Ibañez, L.M., Muruaga, C.M., 2001. Cenozoic evolution of the intramontane Santa María basin, Pampean ranges, northwestern Argentina. J. South Am. Earth Sci. 14 (7), 725–734. https://doi.org/10.1016/S0895-9811(01)00058-X.
Bridge, J., Demicco, R., 2008. Earth Surface Processes, Landforms and Sediment Deposits. Cambridge University Press.
Chen, Y.-W., Wu, J., Suppe, J., 2019. Southward propagation of Nazca subduction along the Andes. Nature 565 (7740), 441–447. https://doi.org/10.1038/s41586-018-0860-1.
Coutand, I., Carrapa, B., Deeken, A., Schmitt, A.K., Sobel, E.R., Strecker, M.R., 2006. Propagation of orographic barriers along an active range front: insights from sandstone petrography and detrital apatite fission-track thermochronology in the intramontane Angastaco basin, NW Argentina. Basin Res. 18 (1), 1–26. https://doi.org/10.1111/j.1365-2117.2006.00283.x.
Dal Molin, C.N., Fernández, D., Escosteguy, L.D., 2003. Hoja Geologica 2766-IV, Concepción. Servicio Geológico Minero Argentino. Instituto de Geología y Recursos Minerales.
DeCelles, P.G., Giles, K.A., 1996. Foreland basin systems. Basin Res. 8 (2), 105–123. https://doi.org/10.1046/j.1365-2117.1996.01491.x.
del Papa, C., Hongn, F., Powell, J., Payrola, P., Do Campo, M., Strecker, M.R., et al., 2013. Middle Eocene-Oligocene broken-foreland evolution in the Andean Calchaqui Valley, NWArgentina: insights from stratigraphic, structural and provenance studies. Basin Res. 25 (5), 574–593.
Dickinson, W.R., 1985. Interpreting provenance relations from detrital modes of Sandstones. Provenance Arenites 333–361.
Druitt, T.H., Sparks, R.S.J., 1982. A proximal ignimbrite breccia facies on Santorini, Greece. J. Volcanol. Geotherm. Res. 13 (1–2), 147–171.
England, P., Molnar, P., 1991. Surface uplift, uplift of rocks, and exhumation of rocks: reply [modified]. Geology 19 (10), 1051–1052.
Fisher, R.V., Schmincke, H.-U., 2012. Pyroclastic Rocks. Springer Science & Business Media.
Flowers, R.M., Ehlers, T.A., 2018. Rock erodibility and the interpretation of low-temperature thermochronologic data. Earth Planet. Sci. Lett. 482, 312–323.
Fosdick, J.C., Reat, E.J., Carrapa, B., Ortiz, G., Alvarado, P.M., 2017. Retroarc basin reorganization and aridification during Paleogene uplift of the southern central Andes. Tectonics 36 (3), 493–514. https://doi.org/10.1002/2016TC004400.
Gavriloff, I.J.C., Bossi, G.E., 1992. Revisión general, análisis facial, correlación y edad de las Formaciones San José y Río Salí (Mioceno Medio, provincias de Catamarca, Tucumán y Salta, República Argentina). Acta Geol. Lilloana 17 (2), 5–43.
Georgieff, S.M., Ibañez, L.M., Vides, M.E., Anis, K.B., Nieva, S.M., 2014. Paleógeno y Neógeno de Tucumán: estratigrafía y paleoambientes sedimentarios. Geología de Tucumán, Colegio de Graduados de Ciencias Geológicas de Tucumán, pp. 106–123.
González, O., 2000. Hoja Geológica 2766-11. San Miguel de Tucumán. Servicio Geológico Minero Argentino, SEGEMAR.
González, O., Viruel, M., Mon, R., Tchilinguirian, P., Barber, E., 2000. Hoja Geológica 2766-II San Miguel de Tucumán. Servicio Geológico Minero Argentino, Boletín 245.
Gupta, S., Allen, P.A., 2000. Implications of foreland paleotopography for stratigraphic development in the Eocene distal Alpine foreland basin. GSA Bull. 112 (4), 515–530.
Hain, M.P., Strecker, M.R., Bookhagen, B., Alonso, R.N., Pingel, H., Schmitt, A.K., 2011. Neogene to Quaternary broken foreland formation and sedimentation dynamics in the Andes of NW Argentina (25°S). Tectonics 30 (2), 1–27. https://doi.org/10.1029/2010TC002703.
Halter, W.E., Bain, N., Becker, K., Heinrich, C.A., Landtwing, M., VonQuadt, A., et al., 2004. From andesitic volcanism to the formation of a porphyry Cu-Au mineralizing magma chamber: the Farallón Negro Volcanic Complex, northwestern Argentina. J. Volcanol. Geotherm. Res. 136 (1–2), 1–30. https://doi.org/10.1016/j.jvolgeores.2004.03.007.
Harris, A.C., Kamenetsky, V.S., White, N.C., Steele, D.A., 2004. Volatile phase separation in silicic magmas at Bajo de la Alumbrera porphyry Cu-Au deposit, NW Argentina. Resour. Geol. 54 (3), 341–356.
Hilley, G.E., Coutand, I., 2010. Links between topography, erosion, rheological heterogeneity, and deformation in contractional settings: insights from the central Andes. Tectonophysics 495 (1–2), 78–92. https://doi.org/10.1016/j.tecto.2009.06.017.
Horton, B.K., 2018. Tectonic regimes of the central and southern Andes: responses to variations in plate coupling during subduction. Tectonics 37 (2), 402–429. https://doi.org/10.1002/2017TC004624.
Howard, J.L., 1993. The statistics of counting clasts in rudites: a review, with examples from the upper Palaeogene of southern California. Sedimentology 40, 157–174.
Iaffa, D.N., Sàbat, F., Bello, D., Ferrer, O., Mon, R., Gutierrez, A.A., 2011a. Tectonic inversion in a segmented foreland basin from extensional to piggy back settings: the Tucuman basin in NW Argentina. J. South Am. Earth Sci. 31 (4), 457–474. https://doi.org/10.1016/j.jsames.2011.02.009.
Iaffa, D.N., Sàbat, F., Muñoz, J.A., Mon, R., Gutierrez, A.A., 2011b. The role of inherited structures in a foreland basin evolution. The Metán Basin in NW Argentina. J. Struct. Geol. 33 (12), 1816–1828. https://doi.org/10.1016/j.jsg.2011.09.005.
Iban, Â.M., Bossi, G.E., Georgieff, S.M., Gavriloff, I.J.C., 2001. 2007/2-3 Temps et temporalités des populations. https://doi.org/10.1016/S0895-9811(01)00058-X 14.
Kleinert, K., Strecker, M.R.M.M.R., 2001. Climate change in response to orographic barrier uplift: paleosol and stable isotope evidence from the late Neogene Santa María basin, Northwestern Argentina. Bull. Geol. Soc. Am. 113 (6), 728–742. https://doi.org/10.1130/0016-7606(2001)113 < 0728:CCIRTO > 2.0.CO;2.
Kley, J., Monaldi, C.R., Salfity, J.A., 1999. Along-strike segmentation of the Andean foreland: Causes and consequences. Tectonophysics 301 (1–2), 75–94. https://doi.org/10.1016/S0040-1951(98)90223-2.
Landtwing, M.R., Dillenbeck, E.D., Leake, M.H., Heinrich, C.A., 2002. Evolution of the breccia-hosted porphyry Cu-Mo-Au deposit at Agua Rica, Argentina: progressive unroofing of a magmatic hydrothermal system. Econ. Geol. 97 (6), 1273–1292. https://doi.org/10.2113/97.6.1273.
Löbens, S., Sobel, E.R., Bense, F.A., Wemmer, K., Dunkl, I., Siegesmund, S., 2013. Refined exhumation history of the northern Sierras Pampeanas, Argentina. Tectonics 32 (3), 453–472. https://doi.org/10.1002/tect.20038.
Lovejoy, N.R., Albert, J.S., Crampton, W.G.R., 2006. Miocene marine incursions and marine/freshwater transitions: evidence from Neotropical fishes. J. South Am. Earth Sci. 21 (1–2), 5–13.
Marshall, L.G., Butler, R.F., Drake, R.E., Curtis, G.H., Tedford, R.H., 1979. Calibration of the Great American interchange. Science 204 (4390), 272–279. https://doi.org/10.1126/science.204.4390.272.
Miall, A.D., 2013. The Geology of Fluvial Deposits: Sedimentary Facies, Basin Analysis, and Petroleum Geology. Springer.
Mon, R., Urdaneta, A., 1972. Introducción a la geología de Tucumán, República Argentina. Rev. Asoc. Geol. Argent. 27 (3), 309–329.
Mortimer, E., Carrapa, B., Coutand, I., Schoenbohm, L., Sobel, E.R.R., Gomez, J.S.S., Strecker, M.R., 2007. Fragmentation of a foreland basin in response to out-of-sequence basement uplifts and structural reactivation: el Cajón - Campo del Arenal basin, NW Argentina. Bull. Geol. Soc. Am. 119 (5–6), 637–653. https://doi.org/10.1130/B25884.1.
Mudelsee, M., Bickert, T., Lear, C.H., Lohmann, G., 2014. Reviews of Geophysics Cenozoic climate changes : a review based on time series analysis of marine benthic δ 18 O records. Rev. Geophys. 52, 333–374. https://doi.org/10.1002/2013RG000440. Received.
Mulder, T., 2011. Gravity processes and deposits on continental slope, rise and abyssal plains. In: first ed. Developments in Sedimentology, vol. 63. Elsevier, pp. 25–148. https://doi.org/10.1016/B978-0-444-53000-4.00002-0.
Muruaga, C.M., 2001. Estratigrafía y desarrollo tectosedimentario de los sedimentos terciarios en los alrededores de la Sierra de Hualfín , borde suroriental de la Puna , Catamarca , Argentina. Revista de La Asociación Argentina de Sedimentología 8 (1), 1–25.
NASA, 1997. Tropical Rainfall Measuring Mission (TRMM). Retrieved from. https://trmm.gsfc.nasa.gov/.
Nichols, G., 2009. Sedimentology and Stratigraphy. (second). UK.
Oncken, O., Hindle, D., Elger, K., Oncken, O., Hindle, D., Kley, J., et al., 2006. The Andes. Springer. https://doi.org/10.1007/978-3-540-48684-8 January 2006.
Orton, G.J., 1995. Facies models in volcanic terrains: time's arrow versus time's cycle. Sediment. Facies Anal.: Tribute Res. Teach. Harold G. Reading 157–193.
Paton, C., Hellstrom, J., Paul, B., Woodhead, J., Hergt, J., 2011. Iolite: Freeware for the visualisation and processing of mass spectrometric data. J. Anal. At. Spectrom. 26 (12), 2508–2518.
Pingel, H., Alonso, R.N., Mulch, A., Rohrmann, A., Sudo, M., Strecker, M.R., 2014. Pliocene orographic barrier uplift in the southern Central Andes. Geology 42 (8), 691–694.
Pratt, J.R., Schoenbohm, L., Mortimer, E., Schmitt, A., Pratt, J.R., Schoenbohm, L.A., et al., 2008. Basin Compartmentalization in the Sierra Pampeanas of Northwestern Argentina : Case-Study of the El Cajon Basin . Basin Compartmentalization in the Sierra Pampeanas of Northwestern Argentina : Case-Study of the El Cajón Basin.
Pye, K., Tsoar, H., 2008. Aeolian Sand and Sand Dunes. Springer Science & Business Media.
Ramos, V.A., 1999. Plate tectonic setting of the Andean Cordillera. Episodes 22 (3), 183–190. https://doi.org/10.1111/j.1365-2621.2006.01230.x.
Roe, G.H., Stolar, D., Willett, S., 2006. The sensitivity of a critical wedge orogen to

climatic and tectonic forcing. *Tectonics, Climate, and Landscape Evolution*. Geol. Soc. Am. Spec. Pap. 398, 227–239.

Roe, G.H., Whipple, K.X., Fletcher, J.K., 2008. Feedbacks among climate, erosion, and tectonics in a critical wedge orogen. Am. J. Sci. 308 (7), 815–842. https://doi.org/10.2475/07.2008.01.

Ruskin, B.G., Dávila, F.M., Hoke, G.D., Jordan, T.E., Astini, R.A., Alonso, R., 2011. Stable isotope composition of middle Miocene carbonates of the Frontal Cordillera and Sierras Pampeanas: did the Paranaense seaway flood western and central Argentina? Palaeogeogr. Palaeoclimatol. Palaeoecol. 308 (3–4), 293–303. https://doi.org/10.1016/j.palaeo.2011.05.033.

Schmitz, M.D., Bowring, S.A., 2001. U-Pb zircon and titanite systematics of the Fish Canyon Tuff: an assessment of high-precision U-Pb geochronology and its application to young volcanic rocks. Geochem. Cosmochim. Acta 65 (15), 2571–2587.

Schoenbohm, L.M., Carrapa, B., McPherson, H.M., Pratt, J.R., Bywater-Reyes, S., Mortimer, E., 2015. Climate and tectonics along the southern margin of the Puna Plateau, NW Argentina: origin of the late Cenozoic punaschotter conglomerates. Geol. Soc. Am. Mem. 212, 251–260.

Sobel, E.R., Strecker, M.R., 2003. Uplift, exhumation and precipitation: tectonic and climatic control of Late Cenozoic landscape evolution in the northern Sierras Pampeanas, Argentina. Basin Res. 15 (4), 431–451. https://doi.org/10.1046/j.1365-2117.2003.00214.x.

Sobel, E.R., Hilley, G.E., Strecker, M.R., 2003. Formation of internally drained contractional basins by aridity-limited bedrock incision. J. Geophys. Res.: Solid Earth 108 (B7).

Sohn, Y.K., 1997. On traction-carpet sedimentation. J. Sediment. Res. 67 (3), 502–509.

Spagnuolo, C.M., Georgieff, S.M., Rapalini, A.E., 2015. Magnetostratigraphy of the Miocene las Arcas formation, Santa María valley, northwestern Argentina. J. South Am. Earth Sci. 63, 101–113. https://doi.org/10.1016/j.jsames.2015.07.004.

Whipple, K.X., 2009. The influence of climate on the tectonic evolution of mountain belts. Nat. Geosci. 2 (2), 97–104. https://doi.org/10.1038/ngeo413.

Whipple, K.X., Tucker, G.E., 1999. Dynamics of the stream-power river incision model: implications for height limits of mountain ranges, landscape response timescales, and research needs. J. Geophys. Res.: Solid Earth 104 (B8), 17661–17674.

Wiedenbeck, M., Alle, P., Corfu, F., Griffin, W.L., Meier, M., Oberli, F. v, et al., 1995. Three natural zircon standards for U-Th-Pb, Lu-Hf, trace element and REE analyses. Geostand. Newsl. 19 (1), 1–23.

Willett, S.D., 1999. Orogeny and orography: the effects of erosion on the structure of mountain belts. J. Geophys. Res.: Solid Earth 104 (B12), 28957–28981.

Zapata, S., Sobel, E.R., del Papa, C., 2018. Influence of inherited structures in along-strike segmentation of the foreland basins in the Central Andes. In: EGU General Assembly Conference Abstracts, vol. 20. pp. 7226.

Zhou, R., Schoenbohm, L.M., Sobel, E.R., Davis, D.W., Glodny, J., 2017. New constraints on orogenic models of the southern Central Andean Plateau: Cenozoic basin evolution and bedrock exhumation. Bull. Geol. Soc. Am. 129 (1–2), 152–170. https://doi.org/10.1130/B31384.1.